

The effect of shear strength on the ballistic response of laminated composite plates

Karthikeyan K.¹, B. P. Russell¹, N.A. Fleck¹, H.N.G. Wadley² and V.S. Deshpande¹

¹Department of Engineering, University of Cambridge, Trumpington Street, Cambridge CB2 1PZ, UK

²Department of Material Science & Engineering, School of Engineering and Applied Science, University of Virginia Charlottesville, VA 22903, USA

26 November 2012

Abstract

The ballistic performance of clamped circular carbon fibre reinforced polymer (CFRP) and Ultra High Molecular Weight Polyethylene (UHMWPE) fibre composite plates of equal areal mass and 0/90° lay-up were measured and compared with that of monolithic 304 stainless steel plates. The effect of matrix shear strength upon the dynamic response was explored by testing: (i) CFRP plates with both a cured and uncured matrix and (ii) UHMWPE laminates with identical fibres but with two matrices of different shear strength. The response of these plates when subjected to mid-span, normal impact by a steel ball was measured via a dynamic high speed shadow moiré technique. Travelling hinges emanate from the impact location and travel towards the supports. The anisotropic nature of the composite plate results in the hinges travelling fastest along the fibre directions and this results in square-shaped moiré fringes in the 0/90° plates. Projectile penetration of the UHMWPE and the uncured CFRP plates occurs in a progressive manner, such that the number of failed plies increases with increasing velocity. The cured CFRP plate, of high matrix shear strength, fails by cone-crack formation at low velocities, and at higher velocities by a combination of cone-crack formation and comminution of plies beneath the projectile. On an equal areal mass basis, the low shear strength UHMWPE plate has the highest ballistic limit followed by the high matrix shear strength UHMWPE plate, the uncured CFRP, the steel plate and finally the cured CFRP plate. We demonstrate that the high shear strength UHMWPE plate exhibits Cunniff-type ballistic limit scaling. However, the observed Cunniff velocity is significantly lower than that estimated from the laminate properties. The data presented here reveals that the Cunniff velocity is limited in its ability to characterise the ballistic performance of fibre composite plates as this velocity is independent of the shear properties of the composites: the ballistic limit of fibre composite plates increases with decreasing matrix shear strength for both CFRP and UHMWPE plates.

Keywords: *plates, ballistic limit, dynamic loading, scaling laws, composites.*

1. Introduction

Structures made from fibre composites are finding increasing application in light-weight ships, vehicles and aircraft. In addition to their structural performance, ballistic resistance may also be a requirement. The projectiles might be fragments and other such threats that are directed at vehicles in military applications, or fragments from roads or runways and other debris in commercial and civilian applications. The fibre composites used for ballistic applications are typically Carbon Fibre Reinforced Polymer (CFRP) composites which primarily serve a structural function but also are expected to provide ballistic protection. Kevlar and other aramid composites, and more recently composites made from Ultra High Molecular Weight Polyethylene (UHMWPE) fibres, are increasingly used for impact resistance but these tend to be parasitic in weight and serve little structural function.

Ultra High Molecular Weight Polyethylene (UHMWPE) fibres were commercialised in the late 1970s by DSM Dyneema, NL under the trade name Dyneema[®] and more recently by Honeywell in the USA under the name Spectra. Both fibres have densities less than that of water ($\rho_f = 970 \text{ kg m}^{-3}$) and tensile strengths in excess of 3 GPa [1]. Their very high specific strength has led to their use in high performance sails, fishing lines and marine mooring cables, and woven fabrics are used to make protective gloves. A rationale for their use in ballistic applications has been presented by Cunniff [2]. Cunniff [2] argued that the ballistic limit of fibre composites scales linearly with the so-called Cunniff velocity c^* of the fibre as defined by

$$c^* = \left(\frac{\sigma_f \varepsilon_f}{2\rho_f} \sqrt{\frac{E_f}{\rho_f}} \right)^{1/3} \quad (1.1)$$

where σ_f and ε_f are the tensile failure strength and failure strain of the fibres respectively, while E_f is the tensile modulus of the fibres. Candidate ballistic materials are plotted in Fig. 1 using axes of specific energy absorption and longitudinal wave speed. Contours of constant Cunniff velocity c^* are included in this plot. This metric suggests that Dyneema[®] fibres (SK60, SK76, etc.) and Spectra fibres considerably outperform most other fibres including Kevlar and armour steels, supporting their use in ballistic applications.

A number of studies have been conducted to measure the static [4-12] and dynamic response [13-16] of UHMWPE fibres and composites. For example, Russell et al. [18] have observed that UHMWPE composites have tensile strengths of a few GPa and a shear strength on the order of a few MPa. Moreover, they found that the tensile strength of UHMWPE fibres displays nearly no strain rate dependence for strain rates up to 10^3 s^{-1} . Such measurements have been used to develop continuum models (Grujicic et al. [19, 20], Iannucci and Pope [21]) to enable the modelling of penetration resistance of UHMWPE composites. Penetration calculations performed using such constitutive models [17, 19-21] are able to reproduce observations to varying degrees of success but typically give little insight into the physical basis of the scaling relation as proposed by Cunniff [2]. In an elegant analytical study, Phoenix and Porwal [3] demonstrated that the ballistic limit of composite plates scales with c^* by assuming a membrane stretching deformation and failure mode of the impacted plate.

There is now growing anecdotal evidence that the matrix shear strength (which governs the inter-laminar shear strength) and the consolidation pressure affect the ballistic performance of

UHMWPE composites. For example, Greenhalgh et al. [22] have recently reported a highly detailed fractography study that illustrates the effect of consolidation pressure and shear strength upon the energy absorption and failure mechanisms such as delamination and splitting. However, matrix shear strength does not affect the value of c^* and so any observed dependence of ballistic limit upon shear strength violates Cunniff scaling. To date, no systematic studies that quantify the effect of shear strength upon the deformation and penetration response of composite plates have been reported. This study attempts to address this gap in the literature.

We choose two $0^\circ/90^\circ$ composite laminates with a wide range of matrix shear strength: (i) CFRP and (ii) Dyneema[®] UHMWPE laminate. In each case we vary the shear strength of the composite by changing the matrix properties while keeping the fibre type, volume fraction and thereby the value of c^* fixed. This enables us to investigate whether the Cunniff velocity is sufficient to characterise the deformation and penetration responses of these composites. Results are also presented for the impact response of stainless steel plates of equal areal mass in order to provide a baseline comparison.

2. Materials and properties

Two types of fibre laminates are investigated : (i) UHMWPE laminates as manufactured by DSM¹ and (ii) CFRP laminates as manufactured by Hexcel Composites Ltd.². Two variants of each of these composites were employed and their designations, fibre and matrix types, lay-ups and volume fraction V_f of fibres are listed in Table 1. A brief description of the manufacturing route for these composites is now presented.

DSM Dyneema composites

Two types of $0^\circ/90^\circ$ laminates, with commercial designations HB26 and HB50, were procured from DSM. The two composites are similar in most respects, as seen in Table 1; however, the polyurethane matrix in HB26 is harder than the kraton rubber matrix in the HB50 composite. The composites are manufactured in 3 steps:

Step I: Fibres are produced by a gel-spinning/hot drawing process [23,24]. The UHMWPE is dissolved in a solvent at a temperature of 150°C and the solution is pumped through a spinneret containing a few hundred capillaries in order to form liquid filaments. These liquid filaments are then quenched in water to form a gel-fibre. The gel-fibre is drawn at a strain rate on the order of 1 s^{-1} in hot air (at 120°C), resulting in a highly oriented (crystalline) fibre of diameter $17\text{ }\mu\text{m}$.

Step II: Fibres are aligned into tows, coated in matrix resin solution and are then formed into a $[0^\circ/90^\circ/0^\circ/90^\circ]$ stack. The stack is dried to remove the matrix solvent.

Step III: The $[0^\circ/90^\circ/0^\circ/90^\circ]$ stack is cut, laid-up to the required thickness and hot pressed (20 MPa at 120°C). Bonding of the layers is achieved by the matrix material. The fibre diameter is unchanged by the hot-pressing operation, although a proportion of the fibres change their cross-sectional shape.

¹ DSM Dyneema B.V., Mauritslaan 49, 6129 EL Urmond, The Netherlands

² Hexcel Composites Ltd., Ickleton Road Cambridge CB22 4QD

CFRP laminates

CFRP prepreg, comprising unidirectional IM7 carbon fibres in an epoxy resin (fiberite 934), was obtained from Hexcel Composites Ltd., and is denoted by the tradename Hexply® 8552/33%/134/IM7 (12K). Two composites, with identical lay-ups as detailed in [Table 1](#), were manufactured. The so-called cured composite was subjected to the standard cure cycle for this resin system (2 hours at 120°C, held under 600 kPa pressure) and is labelled CFRP-C. The uncured composite was left in its pre-preg state and was stored at -15°C; it is termed CFRP-U, and was thawed at room temperature for 5 hours prior to testing.

In addition, 0.71 mm thick cold-rolled 304 stainless steel plates were subjected to quasi-static and ballistic testing, to provide a reference material against which the performance of the composite systems can be compared. All plates (steel and composite) had an areal mass of approximately 5.89 kg m⁻² with plate thicknesses as summarised in [Table 1](#).

2.1 Measurement of material properties

Standard dog-bone shaped specimens were used to measure the uniaxial tensile response of the 304 stainless steel at an applied strain rate of 10⁻³s⁻¹. A more comprehensive series of tests were conducted on the four 0°/90° composites:

- (i) Uniaxial tensile tests were performed in the 0°/90° orientation such that the 0° plies were aligned with the tensile axis. The UHMWPE and CFRP-U laminates have a high tensile strength along the fibre directions, but a very low shear strength (both in-plane and out-of-plane). Thus, a standard tabbed tensile specimen cannot be used to measure the stress versus strain response of a 0°/90° composite. Here, we follow the approach of [Russell et al. \[18\]](#) and make use of a specimen with a large gripping area and a narrow gauge length, as sketched in [Fig. 2a](#). The tensile tests were conducted in a screw driven test machine at a nominal applied strain rate of 10⁻³s⁻¹ with the nominal stress determined from the test machine load cell. The axial nominal strain was measured using a clip gauge of gauge length 12.5 mm. For the CFRP-C composites, tensile tests were conducted as per the ASTM standard [D3039](#) at an applied strain rate of 10⁻³s⁻¹.
- (ii) Tensile tests were performed on the composites with fibres aligned in the ±45° orientation with respect to the tensile axis. While no special specimen geometries were needed, we use the same specimen geometries and procedure as those employed for the 0°/90° tensile tests.
- (iii) Double-notch shear tests were used to measure the inter-laminar shear response, see [Fig. 2b](#). These tests were conducted using the double-notch specimen geometries [\[25,26\]](#) as modified to suit the extreme anisotropy of the composites considered. Specifically, strips of length 150 mm, width $b = 20$ mm and thickness $h = 6$ mm were cut from the UHMWPE and the uncured CFRP sheets. Inter-laminar shear deformation was promoted over a gauge length of length $l = 30$ mm by drilling one hole and 2 notches over the central section of the specimen, as sketched in [Fig. 2b](#). Care was taken to ensure that the hole/notches were positioned so that no fibres spanned the entire length of the specimen. The tests were conducted by friction gripping the specimen ends and pulling them as indicated in [Fig. 2b](#) in a screw driven test machine at a displacement rate of 1 mm/min and 500 mm/min. The inter-laminar shear stress τ_{zx} was defined as $\tau_{zx} \equiv P / (2lb)$, where P is the

measured tensile load and the factor of 2 accounts for the fact that shear loading occurs over 2 inter-laminar planes, as shown in Fig. 2b. The shear displacement across the inter-laminar planes was measured by mounting a clip gauge on either side of the notch as indicated in Fig. 2b. The above procedure was used to measure the inter-laminar shear properties of the HB26, HB50 and CFRP-U composites. In contrast, the CFRP-C composite has a high shear strength and preliminary double-notch tests resulted in a mode-II fracture of the specimen. We conclude that the double-notch shear test is not suitable for extraction of the inter-laminar shear stress versus displacement response.

The tensile stress versus strain curves of the UHMWPE and CFRP laminates in the $0^\circ/90^\circ$ are plotted in Fig. 3a along with that of the 304 stainless steel. In this orientation, all the composites display an approximately elastic-brittle response as the behaviour is dominated by the fibres. Hence, the HB26 and HB50 UHMWPE composites have similar responses, as do the cured and uncured CFRP composites. In contrast, the 304 stainless steel has a strongly hardening elastic-plastic response; the tensile ductility of the 304 stainless steel is about 60% but for the sake of clarity we truncate the data in Fig. 3a at a tensile strain of 2%.

The tensile responses of the CFRP and UHMWPE composites in the $\pm 45^\circ$ orientations, are plotted in Figs. 3b through to 3d, again for a strain rate of 10^{-3}s^{-1} . The responses are now dominated by matrix shear. Hence, the strength of the composites is significantly lower than in the $0^\circ/90^\circ$ orientation and the composites exhibit a higher ductility in the $\pm 45^\circ$ orientation. The HB26, HB50 and the CFRP-U composites have a relatively soft matrix and display considerable ductility (in excess of 20%) and we first consider these materials. After initial yield (denoted by σ_y in Fig. 3), the composites continue to deform by scissoring of the fibres oriented at $\pm 45^\circ$ with respect to the tensile axis. The resulting rotation of the fibres aligns them towards the tensile axis. This gives rise to a geometric hardening response as seen in Figs. 3b and 3c, with the composites finally failing by matrix cracking and the fibres remaining intact. The CFRP-U and HB50 composites have similar strengths while the HB26 composite (which has a stronger matrix) exhibits a higher strength but lower ductility. On the other hand the CFRP-C composite (Fig. 3d) displays a nearly elastic perfectly plastic response with a significantly higher strength of approximately 160 MPa and a relatively low ductility of 4%. The CFRP-C composite also fails by matrix cracking with no fibre rupture.

The inter-laminar shear response of the composites that possess a “soft” matrix (i.e. uncured CFRP, HB26 and HB50) are plotted in Fig. 4 for displacement rates of 1 mm/min and 500 mm/min of the double-notch shear tests. In each case, the measured shear response has considerable rate dependence. Also, the peak shear strength, as measured in the inter-laminar shear test is approximately half the initial tensile yield strength of composites in the $\pm 45^\circ$ orientation; compare Figs. 3 and 4. We emphasise, however, that this test cannot be used to characterise the strength versus shear strain rate dependence of the composites as shall be made clear subsequently. ???

3. Ballistic test protocol

A sketch of the experimental set-up is shown in Fig. 5a. A gas-gun of barrel length 4.5 m and bore diameter 13 mm was used to accelerate the projectiles. Unless otherwise specified,

chrome steel spheres (AISI 52100) of diameter $D = 12.7$ mm and mass $M = 8.3 \times 10^{-3}$ kg were used to impact the plates at velocities V_0 ranging 25 ms^{-1} to 555 ms^{-1} . These projectiles impacted the test plate centre at zero obliquity. A set of laser gates situated at the end of the barrel was used to measure the velocity of the projectile as it exits the barrel.

Square test plates of side length 150 mm were clamped between a front annular steel ring and a steel backing plate, see Fig. 5a. The front annular ring was of inner diameter 100mm, outer diameter 150mm, and thickness 6.35mm. Likewise, the backing plate was of thickness 6.35mm and contained a concentric inner hole of diameter 100mm. In order to mount the backing plate onto an outer frame, the backing plate was machined to a square shape of side length 250mm. Twelve equi-spaced holes of 6 mm diameter were drilled through the test plates on a pitch radius 62.5 mm, to enable the specimens to be sandwiched between the clamping rings. Given the anisotropic nature of the $0^\circ / 90^\circ$ laminates, care was taken to orient these rings such that one set of fibres was aligned with two diametrically opposite bolts.

A range of measurements are summarised as follows:

(i) *Ballistic limit velocity V_L* : For each type of plate, there exists a limiting projectile velocity V_L to prevent plate penetration: a small increase in impact velocity V_0 will result in penetration of the plate. This limiting velocity was determined to an accuracy of 5 ms^{-1} by performing a series of tests at impact velocities V_0 in the vicinity of V_L . In most cases, failure/penetration of the plates was clearly seen after the test. However, in the case of the CFRP-C specimens, elastic spring-back resulted in closure of the hole due to the penetrated projectile. This could lead to the misinterpretation that the plate had survived the impact event, if the judgement was made on post-test inspection of the plate. Furthermore, spallation from the back of the CFRP-C composite plates made it difficult to judge via high speed photography whether the projectile had penetrated. A corrugated cardboard “witness” plate was placed 20 cm behind the CFRP-C plates in order to reveal whether penetration had occurred.

(ii) *The rebound velocity V_R* : The rebound velocity of the steel ball, for impacts velocities $V_0 < V_L$, was measured via high speed photography using a Phantom V12 Camera with an inter-frame time of $12 \mu\text{s}$ and an exposure time of $0.3 \mu\text{s}$. We report this rebound velocity in terms of a coefficient of restitution $e \equiv |V_R / V_0|$.

(iii) *Deflected profile measurements*: Dynamic shadow moiré was used to record the dynamic full field out-of-plane deformation profiles of the rear faces of the plates impacted at $V_0 < V_L$. Details of this technique are given in Lee et al. [27] and Espinosa et al. [28]. Briefly, the set-up for the dynamic shadow moiré measurements is sketched in Fig. 5b and involves lighting of the target by a 100 mm diameter collimated laser beam (of wavelength 532 nm) via a master grating, and observing the interference fringe patterns via high speed photography with an inter-frame time of $11.8 \mu\text{s}$ and an exposure time $0.3 \mu\text{s}$. Lee et al. [27] provide details of the calibration procedure to extract the deflections from the fringe patterns. The gratings used in these experiments resulted in an interference pattern such that each fringe corresponds to an out-of-plane deflection in the range of 0.67 mm - 1.58 mm. **UNCLEAR – ARE A NUMBER OF DIFFERENT GRATINGS USED TO GIVE THIS RANGE IN DEFLECTION INCREMENTS??** An example of the observed fringe patterns for the deformed

HB26 plate impacted at $V_0 = 250 \text{ ms}^{-1}$ is shown in Fig. 6 with an inter-frame time approximately $23 \mu\text{s}$, with time $t = 0$ corresponding to the instant of impact. The fringes reveal that the deflection profiles are not circular due to the anisotropic nature of the $0^\circ / 90^\circ$ HB26 laminate. Also, note that the fringes are observed over approximately $3/4^{\text{th}}$ of the plate as we focussed the laser beam over part of the plate in order to enhance the light intensity and improve the image quality. Note that the symmetry of the material and loading configuration are such that it suffices to measure the deflection over a quarter of the plate in order to reconstruct the full field deformation profiles.

- (iv) *X-ray tomography*: X-ray computed tomography (CT-scan) was employed to visualise the damage in the impacted plates using an X-Tek 160 kV CT scanner.

4. Impact response of plates

The maximum mid-span deflection δ_{max} of the rear face of the plates is plotted as a function of projectile velocity V_0 in Fig. 7a. The ballistic limit V_L is indicated in the figure by an upward arrow (indicating that deflections are unbounded above this velocity). Additionally, the ballistic limit of the five plate types (all of areal mass of 5.89 kg m^{-2} and impacted by the 8.3 g steel ball) is summarised in the bar chart in Fig. 7b.

We consider first the rear-face deformation of the CFRP and steel plates, as deduced from the shadow moiré measurements. (The deformation/failure of the front face is discussed in Section 4.1 where penetration mechanisms are discussed.) Snapshots showing the moiré interference fringes for impact at $V_0 = 54 \text{ ms}^{-1}$ are included in Figs. 8a, 8b and 8c for the steel, CFRP-C and CFRP-U plates, respectively, at selected times t ; the time $t = 0$ is the instant of impact. Note that distortion of the fringe pattern (non-concentricity) is a result of the obliquity of the camera position. **This is corrected for by calibration plates – WHAT DOES THIS MEAN??. STEEL PLATES? DETAILS?** Recall that only about $3/4$ of the target is illuminated and hence the right hand side of the snapshots is dark. Also included in the first image in each case are diametrical lines labelled as 0° and 45° : for the composite plates the 0° line corresponds to a fibre direction in the $0^\circ / 90^\circ$ laminate. Given the symmetry of loading and of the composites, it suffices to analyse only the segment between the 0° and 45° lines in order to reconstruct the deformation of the entire plate. Moiré fringes emanate from the impact location and travel towards the supports. The isotropy of the steel plates results in circular fringes while square-shaped fringes form in $0^\circ / 90^\circ$ laminates; the diagonals of the squares are along the stiff, fibre directions. In the CFRP laminates, the deformation pattern is altered from a square shape at the centre of the plate to a circular pattern adjacent to the circular supports due to the constraint of the supports. Recall from Fig. 7a that the CFRP-C plates undergo a smaller deflection than the CFRP-U and steel plates at any given impact velocity. Consistent with this we observe in Fig. 8 that the fringe spacing is approximately the same for the CFRP-U and steel plates, whereas the fringes are spaced further apart in the CFRP-C plates.

The deflected cross-sectional profiles of the plates along the 0° section (see Fig. 8) are included in Figs. 9a, 9b and 9c for the steel, CFRP-C and CFRP-U plates, respectively at selected times t . Here r is the radial co-ordinate measured from the centre of the plate and z is the out-of-plane co-ordinate. There is insufficient Moiré fringe resolution to allow for a

determination of the deformation profile for $r < 5$ mm and an estimated profile in that region is given by dashed lines; a cubic spline interpolation through the available data is employed, along with the additional constraint that $\partial z / \partial r = 0$ at $r = 0$. In all cases, a travelling hinge emanates from the impact location and propagates towards the supports. We define the location of the travelling hinge r_{hinge} as the radius where the interpolated deflected profile first intersects $z = 0$. The temporal evolution of r_{hinge} for the steel, CFRP-C and CFRP-U plates impacted at $V_0 = 54 \text{ ms}^{-1}$ is shown in Fig. 10. For the CFRP plates, the values of r_{hinge} along both the 0° and 45° cross-sections, as defined in Fig. 8, are included to illustrate the anisotropy of response. The key observations from these figures are:

- (i) The hinge velocity \dot{r}_{hinge} is approximately constant for $r < 30$ mm for all plates and is given in Fig. 10. As the hinges approach the supports, the hinge velocity decreases.
- (ii) The CFRP-C plate has the highest hinge velocity; \dot{r}_{hinge} along the 0° section of the CFRP-U plate is approximately equal to hinge velocity of the steel plate.
- (iii) Recall that the fringes in the CFRP plates have a square shape early in the deformation history. Consistent with this we observe in Figs. 10b and 10c that \dot{r}_{hinge} along the 0° section is approximately a factor of $\sqrt{2}$ greater than \dot{r}_{hinge} along the 45° section during the early stages of plate deformations.

Next, consider the deflections of the rear faces of the UHMWPE and CFRP-U plates subjected to a projectile impact at $V_0 \geq 250 \text{ ms}^{-1}$. These impact velocities exceed the ballistic limit of the steel and CFRP-C plates and hence these plates are omitted from the following discussion. Snapshots showing the moiré interference fringes for an impact with $V_0 = 250 \text{ ms}^{-1}$ are given in Figs. 11a, 11b and 11c for the HB26, HB50 and CFRP-U plates, respectively, at selected times t . Again, lines indicating the 0° and 45° sections are marked on the images. The observations are similar to those made for the low velocity impact of the CFRP-U plate as discussed above. The main difference is that the fringes are more closely spaced in Fig. 11 compared to Fig. 8: the higher velocity impact results in a larger deflection and, in turn, to a higher density of fringes. The deflected profiles of the plates along the 0° section are included in Fig. 12 at selected times t for an impact velocity $V_0 = 250 \text{ ms}^{-1}$ while the variation of the hinge position r_{hinge} with t is plotted in Fig. 13. The evolution of hinge position $r_{hinge}(t)$ along both 0° and 45° sections are given in Fig. 13 for selected impact velocities below the ballistic limit for the HB26, HB50 and CFRP-U plates. (Recall that an impact velocity of 360 ms^{-1} is above the ballistic limit of the CFRP-U plate and hence shadow moiré measurements were not performed at this velocity in order to prevent damage to the associated instrumentation). First, consider the CFRP-U data as shown in Fig. 10c and Fig. 13c. It is clear that the hinge velocity \dot{r}_{hinge} is not strongly influenced by the magnitude of the impact velocity V_0 over the range $V_0 = 54 \text{ ms}^{-1} - 250 \text{ ms}^{-1}$. Given that the moiré fringes in the initial stages have a square shape, the hinge velocity along the 0° and 45° sections differs by a factor of $\sqrt{2}$. These conclusions also apply to the HB26 and HB50 plates from the data shown in Figs. 13a and 13b, respectively.

In a recent study, Karthikeyan et al. [29] have investigated the response of UHMWPE laminate beams to impact by metal foam projectiles; they observed travelling hinges due to inter-laminar shear. Given this, it is intriguing to note that the hinge velocities for all the three plate types shown in Fig. 13 are approximately equal: while the quasi-static inter-laminar shear properties of the HB50 and CFRP-U systems are similar, the HB26 is much stiffer and stronger. The reasons for the weak dependence of hinge velocity upon impact velocity and material properties remain unclear, and are a topic for future investigation.

4.1 Penetration mechanisms

X-ray computed tomography (CT-scan) images of the impacted UHMWPE and CFRP-U plates are shown in Fig. 14 for impact velocities ranging from low values, at which damage is negligible, to velocities exceeding the ballistic limit. The images show a diametrical section (along 0°) through the plates, with the direction of impact marked in Fig. 14a. Note that the spherical steel projectile remained within the CFRP-U plates in some cases and is seen as a circular outline in the CFRP-U images. The corresponding images for the CFRP-C and steel plates are given in Figs. 15 and 16.

Penetration mechanisms of the UHMWPE and CFRP-U plates

The UHMWPE and CFRP-U plates have a qualitatively similar penetration mechanism that is summarised as follows:

- (i) Below a critical velocity V_{crit} the plates deform with no signs of fibre fracture and little or no delamination.
- (ii) At V_{crit} a few plies in contact with the projectile fail by fibre fracture and delaminate from the remainder of the plate. The unfractured portion of the plate remains intact with little or no delamination inside it.
- (iii) At the ballistic limit V_L all plies have failed at the projectile impact location, thereby allowing the projectile to penetrate the plate. Extensive de-lamination is observed throughout the plate.

This progressive sequence of ply fracture is quantified in Fig. 17 where we plot the fraction η of fractured plies as a function of normalized impact velocity $\bar{V}_0 \equiv V_0 / V_L$. For the UHMWPE and CFRP-U plates, ply fracture starts at $V_{crit} \approx 0.5V_L$, with $\eta = 1$ at $V_0 = V_L$, illustrating that penetration occurs by the progressive failure of plies up to the ballistic limit.

Penetration mechanisms of the CFRP-C plates

The penetration process is rather different for the CFRP-C plate, and we discuss this with reference to the images in Fig. 15a. Again, below a certain critical velocity there is no observable damage in terms of delamination or fibre fracture. However, at a critical velocity ($V_{crit} \approx 69 \text{ ms}^{-1}$ for the CFRP-C plate) fibre fracture occurs through the entire plate thickness, along with delamination throughout the plate thickness. Moreover, even though all plies have fractured at V_{crit} the projectile has not penetrated the plate. Based on these observations we propose the following sequence of events for impact velocities in the range $V_{crit} < V_0 < V_L$:

- (i) The projectile impacts the plate and transmits some momentum into the plate.
- (ii) A cone crack develops in the plate similar to those seen in the indentation of monolithic ceramics; see the high magnification X-ray micrograph in Fig. 15b of a diametrical section of the plate impacted at $V_0 = 69 \text{ ms}^{-1}$. This crack initiates

while the projectile is in contact with the plate or after the projectile has rebounded. The experiments here are unable to differentiate between these two possibilities.

At and above the ballistic limit, i.e. $V_0 \geq V_L$ the projectile penetrates the plate and from the image at $V_0 = 206 \text{ ms}^{-1}$ in Fig. 15a we infer the following failure sequence:

- (i) The high velocity projectile comminutes the fibres within the plies on the impacted face, as evidenced from the missing plies on this face for the $V_0 = 206 \text{ ms}^{-1}$ case, see Fig. 15a. This bears some resemblance to the comminuted zone in a ceramic, see for example REF??.
- (ii) The projectile continues to penetrate the plate and the plate enters a bending deformation phase.
- (iii) Plate bending results in tensile fibre fracture and consequently the projectile can penetrate the plate.

The qualitative difference in penetration processes for the CFRP-C plates and for the CFRP-U and UHMWPE plates is further seen by comparing the η versus \bar{V}_0 responses in Fig. 17. For the case of CFRP-C, η is a step function that rises from zero to unity at $V_0 = V_{crit} \approx 0.5V_L$. We conclude that penetration in the CFRP-C plates is not a consequence of gradual failure of plies as observed for the cases of CFRP-U and UHMWPE.

Penetration mechanisms of the steel plates

Consider again the progressive deformation and failure of the steel plate, as reported in Fig. 16. There are no obvious signs of damage/failure for $V_0 < 196 \text{ ms}^{-1}$. At $V_0 = 196 \text{ ms}^{-1}$ sheet necking occurs; this is manifested in the X-ray images by the lightening of the image as the necked/thinned material is more X-ray transparent than the remainder of the plate. At the ballistic limit ($V_0 = V_L = 206 \text{ ms}^{-1}$) this neck results in fracture of the material and the projectile penetrates the plate, leaving behind a cusp of material still attached to the plate, as seen in the final image of Fig. 16.

We conclude that significant inelastic processes occur in the steel, CFRP-U and UHMWPE plates for impact velocities $V_0 < V_L$ while the response of the CFRP-C plates is nearly elastic up to the velocity $V_0 = V_L$ (although some inelastic processes do occur in the form localised fibre fracture for $V_0 > V_{crit}$). This manifests itself in terms of the rebound velocities of the projectile measured via high speed photography. We plot in Fig. 18 the effective coefficient of restitution e as a function of \bar{V}_0 . Here, we define the effective coefficient of restitution as $e \equiv -V_R / V_0$, where V_R is the rebound velocity of the projectile and has the opposite sign to the incoming projectile velocity V_0 . It is clear that e for the CFRP-C plates is significantly higher than that for the other plates and only starts to drop for $\bar{V}_0 > 0.9$. The steel plates have an intermediate value of e while the UHMWPE and CFRP-U plates give rise to low values of rebound velocity ($e \approx 0.1$) over a wide range $0 < \bar{V}_0 < 0.8$. For values of $1 > \bar{V}_0 > 0.8$, e drops to zero for the UHMWPE and CFRP-U plates. In these cases, the projectile becomes trapped within these laminates (recall Fig. 14c).

5. Cunniff scaling

Cunniff [2] argued via dimensional analysis and comparisons with experimental data that the ballistic limit V_L of plates made from fibrous composite materials (e.g. CFRP, GFRP, Kevlar composites, UHMWPE composites, etc.) is given by a relation of the form

$$\frac{V_L}{\hat{c}} = f\left(\frac{m_{plate}}{m_{projectile}}\right) \quad (5.1)$$

where m_{plate} is the areal mass of the plate and $m_{projectile}$ is the areal mass of the projectile (defined as the ratio of the mass of the projectile and its projected area on the plate). In his analysis, Cunniff viewed the velocity \hat{c} as a material property that characterises the ballistic performance and deduced \hat{c} as follows. He took Kevlar-29 as the reference material, and assumed that $\hat{c} = c^*$ (as defined in equation (1.1)); the functional form of the relation, Eq. (5.1), was obtained by plotting the normalised measured ballistic limit V_L / \hat{c} versus $m_{plate} / m_{projectile}$ for Kevlar-29 composite plates. This curve is taken from [2] and is included in Fig. 19. Next, he plotted the measured values of V_L for a range of other composites and determined the values of \hat{c} in each case such that all the curves lay approximately on the “master-curve” as generated from the Kevlar-29 data. These normalised curves are reproduced from Cunniff [2] in Fig. 19 and the associated values of \hat{c} and c^* values are listed in Table 2.

The values for V_L and $m_{plate} / m_{projectile}$ for the composite plates of the present study are taken from Fig. 7b and fitted to the master-curve of Fig. 19 in order to deduce the best-fitting values for \hat{c} in each case: we follow the procedure as laid down by Cunniff [2]. These values for \hat{c} are listed in Table 2, along with the c^* values as deduced from equation (1.1). Note that $\hat{c} < c^*$ for the CFRP and UHMWPE composites of the present study, and for most of the composites as considered by Cunniff [2]. This suggests that, in comparison to Kevlar-29, these composites underperform with respect to the membrane-stretching mode as detailed by Phoenix and Porwal [3].

A deficiency with the data presented in [2] is that no information is provided on the basic material properties of the composites, making it difficult to rationalize \hat{c} in terms of more fundamental material properties. We proceed to discuss the additional factors that affect the value of \hat{c} .

5.1 Measurement of the ballistic limit of HB26 as a function of projectile mass

Our measurement of ballistic limit has been restricted, so far, to a single mass ratio $m_{plate} / m_{projectile}$. We proceed to explore the sensitivity of the ballistic limit V_L to the mass ratio, for the HB26 composite, and thereby determine whether the master-curve (5.1), as deduced for Kevlar-29 applies also to HB26. To achieve this, we performed additional ballistic tests on

5.89 kg m⁻² HB26 plates (using the same clamping configuration as described in Section 4) using 4 more projectiles : these have a mass in the range 3 g to 16 g but have the same projected area as that of the 8.3 g projectile as used in Section 4.

Sketches of the 5 projectiles (including the 8.3 g steel ball employed in Section 4) are given in Fig. 20. The projectiles of different masses were constructed as follows:

- (i) The 3 g projectile was a spherical ball of diameter $D = 12.7$ mm made from a 7000 series aluminium alloy.
- (ii) The 4.6 g and 5.4 g projectiles were constructed by first cutting a 8.3 g steel ball into an hemisphere and then adhering the hemisphere to a Nylon backing cylinder, of identical diameter $D = 12.7$ mm and length 9.8 mm, see Fig. 20. While the 5.4 g projectile was adhered to a solid Nylon cylinder, the 4.6 g projectile weight was achieved by hollowing out the Nylon cylinder to reduce the overall weight of the projectile from 5.4 g to 4.6 g.
- (iii) The 16 g projectile was constructed by adhering the steel hemisphere to a steel cylinder of diameter $D = 12.7$ mm and length 12.5 mm, as described in (ii)

The measured values of V_L for the HB26 plate impacted by the five projectiles of different masses have been added to Fig.19 with the choice of $\hat{c} = 672$ ms⁻¹ (the same value as that obtained in the previous section of the paper for HB26). The measurements normalised in this manner lie on the Cunniff [2] master-curve.

5.2 Relation of \hat{c} to composite properties

Phoenix and Porwal [3] analysed the problem of an elastic membrane impacted by a projectile. Using this analysis they calculated the maximum strain (which occurs immediately under the projectile) as a function of impact velocity. By setting this strain equal to the uniaxial failure strain Phoenix and Porwal [3] demonstrated that the ballistic limit of the membrane follows a relation of the form, Eq. (5.1), but with \hat{c} given by c^* as defined in Eq. (1.1) for the effective properties of the laminate rather than for the fibre: Phoenix and Porwal took σ_f , ε_f , E_f and ρ_f to be the effective values of the membrane material. For the sake of clarity, we denote this velocity as \tilde{c} . Thus, \tilde{c} for the HB26 composite can be calculated using the measured laminate properties reported in Section 2. With $\sigma_f = 768$ MPa, $\varepsilon_f = 2\%$, $E_f \equiv \sigma_f / \varepsilon_f$ and $\rho_f = 970$ kgm⁻³, the velocity $\tilde{c} = 391$ ms⁻¹.

This is significantly less than the value of the scaling velocity $\hat{c} = 672$ ms⁻¹ required to collapse the HB26 ballistic data onto the Cunniff [2] master-curve; see Table 2. We note that material strain rate effects cannot rationalise this discrepancy as the measurements of Russell et al. [18] have shown that the tensile response of SK76 Dyneema[®] fibres in the HB26 composite is strain rate insensitive over the relevant range of 100 s⁻¹ to 10³ s⁻¹. We conclude that the Cunniff/Phoenix parameters are insufficient to characterise the ballistic performance of the HB26 composite.

5.3 Cunniff/Phoenix analysis deficiencies

The experimental data presented in this study indicates key drawbacks in using \tilde{c} based on the effective laminate properties to predict the ballistic limit of composite plates. This is clearly seen in Table 2 where we note that the \tilde{c} values are not equal to \hat{c} for any of the composite systems employed in this study, i.e. \tilde{c} does not effectively characterise the

ballistic performance of these composites. We briefly discuss some underlying reasons for this discrepancy.

The ballistic limit as defined by \tilde{c} is independent of the shear stiffness and strength of the laminates. In the results presented in Section 4, we have demonstrated that V_L is strongly dependent on the shear properties. The ballistic limits V_L for the CFRP and UHMPE plates impacted by the 8.3 g steel balls are plotted in Fig. 21 as a function of the measured shear strength τ_y of the composites (in Fig. 21 τ_y is defined to be equal to half the uniaxial tensile strength, σ_y of the composite in the $\pm 45^\circ$ orientation³ for an applied strain rate of 10^{-3} s^{-1} ; see Fig. 3). The CFRP-C and CFRP-U composites have identical values of σ_f , ε_f , E_f and ρ_f as both plates have the same fibre type and volume fraction; the measured values of these parameters (Fig. 3) gives $\tilde{c} = 300 \text{ ms}^{-1}$ for both the CFRP-U and CFRP-C plates. Similarly, the HB26 and HB50 UHMWPE plates have identical values of these material properties, to give $\tilde{c} = 391 \text{ ms}^{-1}$. It is clear from Fig. 21 that V_L increases sharply with decreasing τ_y for both the CFRP and UHMWPE plates even though \tilde{c} remains fixed in both cases. It is insufficient to use just \tilde{c} to characterise the ballistic performance of these plates: \tilde{c} is independent of τ_y while the ballistic limit depends strongly on the shear strength of the composites.

The origins of this discrepancy can be understood by re-examining the Phoenix and Porwal [3] rationalisation of the Cunniff [2] observations. Phoenix and Porwal [3] presented an elegant analysis in an attempt to rationalise the Cunniff [2] observation that the ballistic limit of fibre composite plates scales linearly with \hat{c} . Phoenix and Porwal predicted that V_L scales linearly with \tilde{c} based on the assumption that failure occurs in a membrane-like mode under the projectile. This failure mode is a binary event with all plies of the composite plate failing at an impact velocity V_L . Such a membrane type failure mode is not observed in any of the composite plates tested here: while a brittle cone-like fracture mode involving negligible plate deflections occurs for the CFRP-C plates (Fig. 15), the UHMWPE and CFRP-U plates fail in a progressive manner (Fig. 14) with an increasing number of plies failing with increasing impact velocity until all plies fail at V_L , as discussed in Section 4.1.

We finally note that the parameter introduced by Cunniff [2], labelled \hat{c} here, can be treated as an independent material property that captures the dependence of V_L on the ratios of the areal masses of the plate and projectile. Thus, a single ballistic test to calibrate \hat{c} will enable the prediction of the ballistic limit of the fibre composite plates over a range of projectile/plate masses using the master curve presented in Fig. 19. The dependence of \hat{c} on more fundamental material properties such as shear strength, fibre strength, etc. remains a key research challenge in understanding the ballistic performance of fibre composite systems.

³ Recall that the shear strength as measured in this inter-laminar shear test is approximately half the initial tensile yield strength σ_y of composites in the $\pm 45^\circ$ orientation.

6. Concluding remarks

The impact and ballistic performance of CFRP and Ultra High Molecular Weight Polyethylene (UHMWPE) clamped laminate plates of equal areal mass was measured and compared with that of 304 stainless steel plates. Two grades of UHMWPE and of CFRP composites were employed to study the effect of the shear strength upon the ballistic limit: (i) CFRP plates with both a cured and uncured matrix and (ii) UHMWPE laminates with identical fibres but with matrices of two different shear strengths.

The response of these plates to central, normal impact by a steel ball was measured via a dynamic high speed shadow moiré technique. Travelling hinges initiate at the impact site and travel towards the clamped supports. The isotropic steel plates develop circular moiré fringes, whereas the anisotropy of the composite plates results in the hinges travelling faster in the fibre directions, and this gives rise to square-shaped moiré fringes in the plates. While the deformation behaviours of all plates are broadly similar, the penetration responses are markedly different. Projectile penetration into the UHMWPE and uncured CFRP plates occurs in a progressive manner, such that an increasing number of plies fail in the contact zone of the projectile with increasing velocity. In contrast, the cured CFRP plate fails in a ceramic-like manner with a cone crack forming at lower velocities. At higher velocities cone-cracking is accompanied by the comminution of plies beneath the projectile. The steel plate fails by ductile necking along a circular ring of diameter approximately equal to that of the projectile. On an equal areal mass basis, the low shear strength UHMWPE plate (HB50) has the highest ballistic limit followed by the high strength UHMWPE plate (HB26), the uncured CFRP, the steel plate and finally the cured CFRP plate.

The scaling of the ballistic limit as a function of the projectile mass was measured for the UHMWPE plates of high shear strength. These measurements demonstrated that the ballistic data followed a Cunniff-type scaling. However, the Cunniff velocity required to normalise the ballistic limit velocities was significantly higher than that estimated from the laminate properties. In fact, the data presented here has clearly shown that the ballistic limit for both the CFRP and UHMWPE plate increased with decreasing shear strength: this dependence cannot be captured by the Cunniff scaling as the Cunniff velocity is independent of the composite shear strength. While this study has demonstrated the effect of the composite shear strength on the ballistic performance, no mechanistic models to explain this dependence has, as yet, been proposed. This remains a topic for future research.

Acknowledgments

This research was supported by the Office of Naval Research (ONR NICOP grant number N00014-09-1-0573 **HAS THIS NICOP FINISHED? QUOTE FLECK NICOP?**) as part of a Multidisciplinary University Research Initiative on “Cellular materials concepts for force protection”, Prime Award No. N00014-07-1-0764 is gratefully acknowledged. The program manager was Dr David Shifler. The authors also wish to thank DSM Dyneema for supplying the HB26 and HB50 laminate plates, and technical discussion facilitating the experimental programme. Dyneema® is a trademark of DSM. Dr B. P. Russell was supported by a Ministry of Defence / Royal Academy of Engineering Research Fellowship.

References

- [1] Hearle JWS. High-performance fibres. Woodhead Publishing, 2001
- [2] Cunniff PM. Dimensionless parameters for optimization of textile-based body armor systems, In: Reinecke WG, editor. Proceedings of the 18th International Symposium on Ballistics, San Antonio, TX. Lancaster: Technomic, 1999 p1303-1310.
- [3] Phoenix SL, Porwal PK. A new membrane model for the ballistic impact response and V50 performance of multi-ply fibrous systems. *Int J Solids Struct* 2003;40:6723-65
- [4] Wilding MA, Ward IM. Tensile creep and recovery in ultra-high modulus linear polyethylenes. *Polym* 1978;19:969-76
- [5] Wilding MA, Ward IM. Creep and recovery of ultra high modulus polyethylene. *Polym* 1981;22:870-6
- [6] Wilding MA, Ward IM. Creep and stress-relaxation in ultra-high modulus linear polyethylene. *J Mater Sci* 1984;19:629-36
- [7] Jacobs M, Heijnen N, Bastiaansen C, Lemstra PJ. A novel, efficient route for the crosslinking and creep improvement of high modulus and high strength polyethylene fibres. *Macromol Mater Eng* 2000;283:120-5
- [8] Govaert LE, Lemstra PJ. Deformation behavior of oriented UHMW-PE fibers. *Colloid Polym Sci* 1992;270:455-64
- [9] Peijs A, Catsman P, Govaert LE, Lemstra PJ. Hybrid composites based on polyethylene and carbon fibres Part 2: influence of composition and adhesion level of polyethylene fibres on mechanical properties. *Composites* 1990;21:513-21
- [10] Govaert LE, Bastiaansen C, Leblans P. Stress-strain analysis of oriented polyethylene. *Polym* 1993;34:534-40
- [11] Kromm F, Lorriot T, Coutand B, Harry R, Quenisset JM. Tensile and creep properties of ultra high molecular weight PE fibres. *Polym Test* 2003;22:463-70
- [12] Dessain B, Moulart O, Keunings R, Bunsell AR. Solid phase change controlling the tensile and creep behaviour of gel-spun high-modulus polyethylene fibres. *J Mater Sci* 1992;27:4515
- [13] Huang W, Wang Y, Xia Y. Statistical dynamic tensile strength of UHMWPE-fibers. *Polym* 2004;45:3729-34
- [14] Koh ACP, Shim VPW, Tan VBC. Dynamic behaviour of UHMWPE yarns and addressing impedance mismatch effects of specimen clamps. *Int J Impact Eng* 2010;37:324-32
- [15] Benloulou IC, Rodriguez J, Martinez MA, Galvez VS. Dynamic tensile testing of aramid and polyethylene fiber composites. *Int J Impact Eng* 1997;19:135-46
- [16] Koh C, Shim V, Tan V, Tan B. Response of a high-strength flexible laminate to dynamic tension. *Int J Impact Eng* 2008;35:559-68
- [17] Frissen RJT. Modelling the Ballistic Impact Behaviour of Polyethylene-Fibre-Reinforced Composites. Eindhoven: University of Technology; 1996
- [18] Russell BP, Karthikeyan K, Deshpande VS, Fleck NA. The high strain rate response of Ultra High Molecular-weight Polyethylene: from fibre to laminate. Submitted to *Int J Impact Eng* 2012
- [19] Grujicic M, Glomski PS, He T, Arakere G, Bell WC, Cheeseman BA. Material Modeling and Ballistic-Resistance Analysis of Armor-Grade Composites Reinforced with High-Performance Fibers. *J Mater Eng Perform* 2009;18:1162-82
- [20] Grujicic M, Arakere G, He T, Bell WC, Glomski PS, Cheeseman BA. Multi-scale ballistic material modeling of cross-plyed compliant composites. *Composites Part B* 2009;40:468-82

- [21] Iannucci L, Pope D. High velocity impact and armour design. *Express Polym Lett* 2011;5:262-72
- [22] Greenhalgh ES, Bloodworth VM, Iannucci L, Pope D. Fractographic observations on Dyneema[®] composites under ballistic impact, *Composites Part A*;2013;44:51-62.
- [23] Smith P, Lemstra PJ, Kalb B, Pennings AJ. Ultrahigh-Strength Polyethylene Filaments by Solution Spinning and Hot Drawing. *Polym Bull* 1979;1:733-6
- [24] Smith P, Lemstra P. Ultra-high-strength polyethylene filaments by solution spinning/drawing. *J Mater Sci* 1980;15:505-14
- [25] Daniel IM, Ishai O. *Engineering Mechanics of Composite Materials*, Oxford University Press, New York, Second Ed., 2005.
- [26] Liu G, Thouless MD, Deshpande VS, Fleck NA. Collapse mechanisms of a UHMWPE laminated beam, Submitted to *Int J Solids Struct* 2012.
- [27] Lee S. *Dynamic Failure of Blast-Resistant Structures Subjected to Impulsive Loading*. Evanston, USA:Northwestern University; 2005.
- [28] Espinosa HD, Lee S, Moldovan N. A novel fluid-structure interaction experiment to investigate deformation of structural elements subjected to impulsive loading. *Exp Mech* 2006;46:805-904.
- [29] Karthikeyan K, Russell BP, Fleck NA, O'Masta M, Wadley HNG, Deshpande VS. The soft impact response of composite laminate beams. Submitted to *International Journal of Impact Engineering*.

Figure Captions

Fig. 1: Materials typically used for ballistic protection applications plotted in longitudinal wave speed – specific energy absorption space. Contours of constant Cunniff velocity c^* are included to indicate the best ballistic materials.

Fig. 2: Sketches of the specimens used to measure (a) the tensile responses of the laminates in the $0^\circ/90^\circ$ and $\pm 45^\circ$ orientations and (b) the inter-laminar shear response using a double-notch shear specimen. All dimensions are in mm.

Fig. 3: The measured tensile stress versus strain responses of the (a) CFRP and UHMWPE laminates in the $0^\circ/90^\circ$ orientation as well as the 304 stainless steel. The corresponding responses in the $\pm 45^\circ$ orientation for the (b) HB26, (c) HB50 and CFRP-U and (d) CFRP-C composites. All the response are for an applied strain rate of 10^{-3} s^{-1} . The matrix yield strength is indicated on (b) to (d) by σ_y .

Fig. 4: The measured inter-laminar shear stress τ_{zx} versus applied shear displacement Δ responses of the (a) the HB26, (b) HB50 and (c) CFRP-U laminates at applied displacement rates of 1 mm/min and 500 mm/min. The tests were performed using the double-notch shear specimens sketched in Fig. 2b.

Fig. 5: (a) Plan and side view of the impact test apparatus illustrating the test set-up and the clamping arrangement. (b) Sketch showing the optical set-up used in the dynamic shadow moiré measurements. All dimensions are in mm.

Fig. 6: Example of moiré interference fringe patterns observed during the deformation of the HB26 plate impacted at $V_0 = 250 \text{ ms}^{-1}$ by a 8.3 g steel ball. Time t as measured after the instant of impact is included on each image. Each fringe corresponds of an out-of-plane displacement of 1.58 mm. The fibres are vertically and horizontally aligned.

Fig. 7: The maximum mid-span deflection δ_{\max} of the plate as a function of the impact velocity V_0 of the 8.3 g steel projectile. (b) A summary of the ballistic limit V_L of the 5 plate types tested here impacted by the 8.3 g steel projectile.

Fig. 8: Montages of moiré interference fringes during deformation of the (a) stainless steel, (b) CFRP-C and (c) CFRP-U plates at impacted $V_0 = 54 \text{ ms}^{-1}$ by the 8.3 g steel projectile. Time t as measured after the instant of impact is included on each image and the 0° and 45° sections are marked in the first image in each case. Each fringe corresponds of an out-of-plane displacement of 0.67 mm.

Fig. 9: The measured transient profiles for the (a) stainless steel, (b) CFRP-C and (c) CFRP-U plates along the 0° section. The profiles are extracted from the moiré fringes in Fig. 8 for the plates impacted at $V_0 = 54 \text{ ms}^{-1}$ by the 8.3 g steel ball. Time t as measured after the instant of impact is included on each figure.

Fig. 10: The time evolution of the hinge location r_{hinge} in the (a) stainless steel, (b) CFRP-C and (c) CFRP-U plates impacted at $V_0 = 54 \text{ ms}^{-1}$ by the 8.3 g steel ball. Data is shown for the

CFRP plates along both 0° and 45° sections marked in Fig. 8 with time t as measured after the instant of impact.

Fig. 11: Montages of moiré interference fringes during deformation of the (a) HB26 (b) HB50 and (c) CFRP-U plates at impacted $V_0 = 250 \text{ ms}^{-1}$ by the 8.3 g steel projectile. Time t as measured after the instant of impact is included on each image and the 0° and 45° sections are marked in the first image in each case. Each fringe corresponds of an out-of-plane displacement of 1.58 mm.

Fig. 12: The measured transient profiles for the (a) HB26, (b) HB50 and (c) CFRP-U plates along the 0° section. The profiles are extracted from the moiré fringes in Fig. 11 for the plates impacted at $V_0 = 250 \text{ ms}^{-1}$ by the 8.3 g steel ball. Time t as measured after the instant of impact is included on each figure.

Fig. 13: The time evolution of the hinge location r_{hinge} in the (a) HB26, (b) HB50 and (c) CFRP-U plates impacted by the 8.3 g steel ball at impact velocities indicated in each figure. Data is shown along both 0° and 45° sections marked in Fig. 11 with time t as measured after the instant of impact.

Fig. 14: X-ray images along the diametrical section of the (a) HB26, (b) HB50 and (c) CFRP-U plates impacted by the 8.3 g steel ball at selected impact velocities V_0 . Images are shown for V_0 both below and above the ballistic limit.

Fig. 15: (a) X-ray images along the diametrical section of CFRP-C plates impacted by the 8.3 g steel ball at selected impact velocities V_0 . Images are shown for V_0 both below and above the ballistic limit. (b) A high resolution image of the $V_0 = 69 \text{ ms}^{-1}$ CFRP-C case from (a) showing the formation of a cone crack under the projectile.

Fig. 16: X-ray images along the diametrical section of stainless steel plates impacted by the 8.3 g steel ball at selected impact velocities V_0 . Images are shown for V_0 both below and above the ballistic limit.

Fig. 17: The measured fraction η of broken plies as a function of normalised impact velocity $\bar{V}_0 \equiv V_0 / V_L$ for the UHMWPE and CFRP composite plates.

Fig. 18: The measured co-efficient of restitution e as a function of the normalised impact velocity $\bar{V}_0 \equiv V_0 / V_L$ for the UHMWPE, CFRP and stainless steel plates.

Fig. 19: The ballistic limit V_L of a range of fibre composite plates as a function of the ratio $m_{plate} / m_{projectile}$ of the areal mass of the plate and projectile. The data for V_L is taken from [Cunniff \[2\]](#) and normalised by \hat{c} whose values are listed in Table 2 for each of the composites. The data for HB26 measured from the current study is also included with the normalisation factor $\hat{c} = 672 \text{ ms}^{-1}$.

Fig. 20: Sketches of the 5 projectiles of different masses but equal projected areas used to study the ballistic Cunniff-type scaling of the HB26 composite plates.

Fig. 21: The ballistic limit V_L of the UHMWPE and CFRP composite plates as a function of the shear strength τ_y . The designations of the each of the composites is indicated in the figure.

List of Tables

Table 1: Constituent and construction details for the four laminate material systems.

Laminate	Fibre	Matrix	Lay-up & thickness h	Fibre volume fraction V_f
HB26	SK76 Ø17.0 μm	Polyetherdiol-aliphatic diisocyanate polyurethane	$[0^\circ/90^\circ]_{48}$ $h = 6 \text{ mm}$	0.83
HB50	SK76 Ø15.7 μm	Styrene-isoprene-styrene triblock copolymer	$[0^\circ/90^\circ]_{54}$ $h = 6 \text{ mm}$	0.82
CFRP-C	IM7 Ø 5 μm	Epoxy fiberite 934 (cured – 2 hrs@120°C, 6 Bar)	$[(0^\circ/90^\circ)_7 0^\circ]$ $h = 3.75 \text{ mm}$	0.55
CFRP-U	IM7 Ø 5 μm	Epoxy fiberite 934 (uncured)	$[(0^\circ/90^\circ)_7 0^\circ]$ $h = 4 \text{ mm}$	0.55

Table 2: A comparison between the Cunniff [2] velocity c^* given by Eq. (1.1) and the normalisation velocity \hat{c} required to reduce the ballistic data to a single master curve for a range of composite materials. Data for the Dyneema[®] (HB26 and HB50) and CFRP (CFRP-C and CFRP-U) systems is based on measurements reported here and includes the normalisation velocity \tilde{c} based on the laminate properties. The data for the other material systems is extracted from Cunniff [2].

Material	Cunniff velocity [2]		Normalisation velocity
	$c^* (\text{ms}^{-1})$	$\tilde{c} (\text{ms}^{-1})$	$\hat{c} (\text{ms}^{-1})$
Kevlar [®] 29	625	–	625
Kevlar [®] KM2	682	–	682
Glass	559	–	482
Carbon fibre	593	–	375
Nylon	482	–	482
Spectra [®] 1000	801	–	672
Dyneema [®] SK76 (HB26)	925	391	672
Dyneema [®] SK76 (HB50)	925	391	751
IM7 (CFRP-C)	739	300	146
IM7 (CFRP-U)	739	300	460

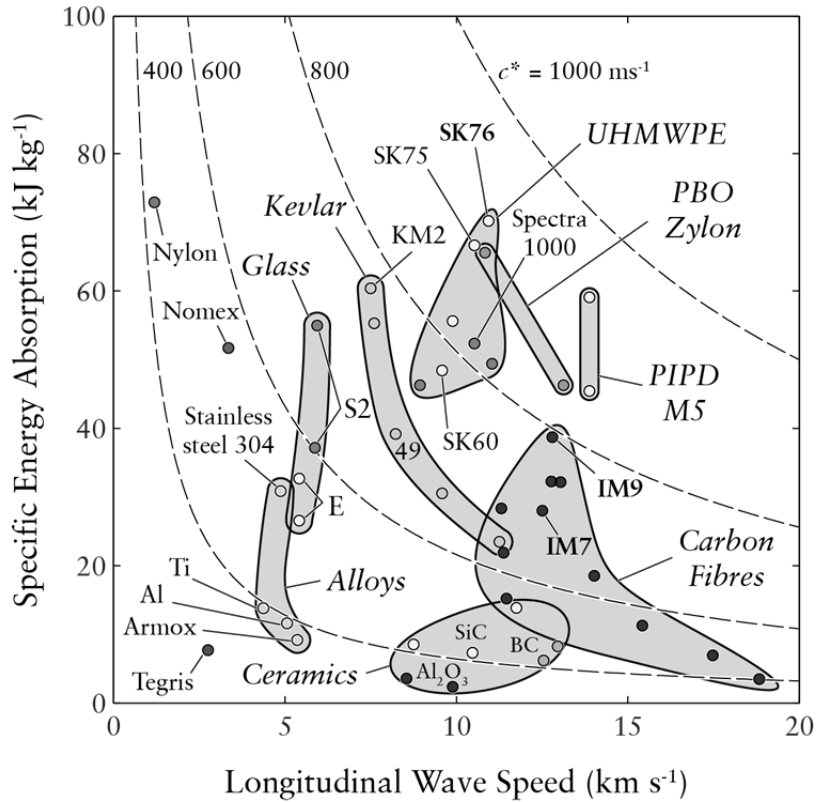


Fig. 1: Materials typically used for ballistic protection applications plotted in longitudinal wave speed – specific energy absorption space. Contours of constant Cunniff velocity c^* are included to indicate the best ballistic materials.

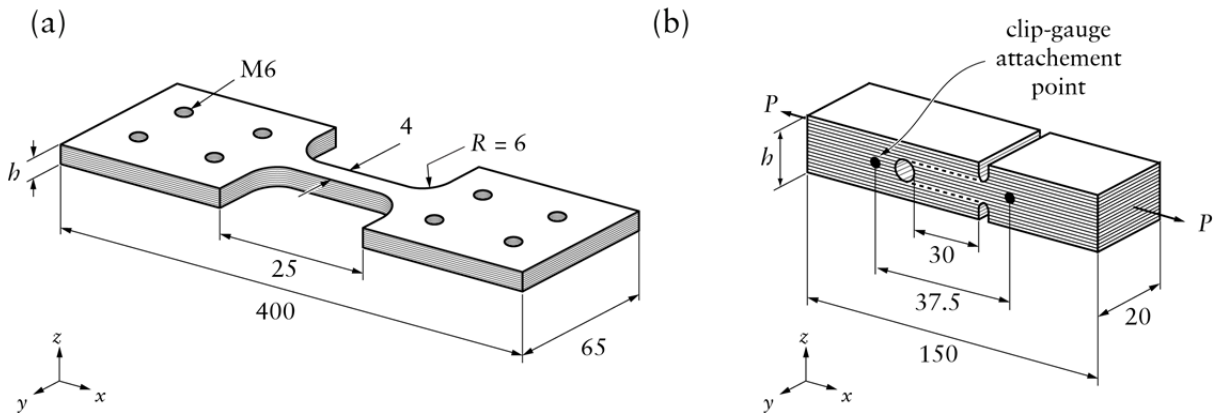


Fig. 2: Sketches of the specimens used to measure (a) the tensile responses of the laminates in the $0^\circ/90^\circ$ and $\pm 45^\circ$ orientations and (b) the inter-laminar shear response using a double-notch shear specimen. All dimensions are in mm.

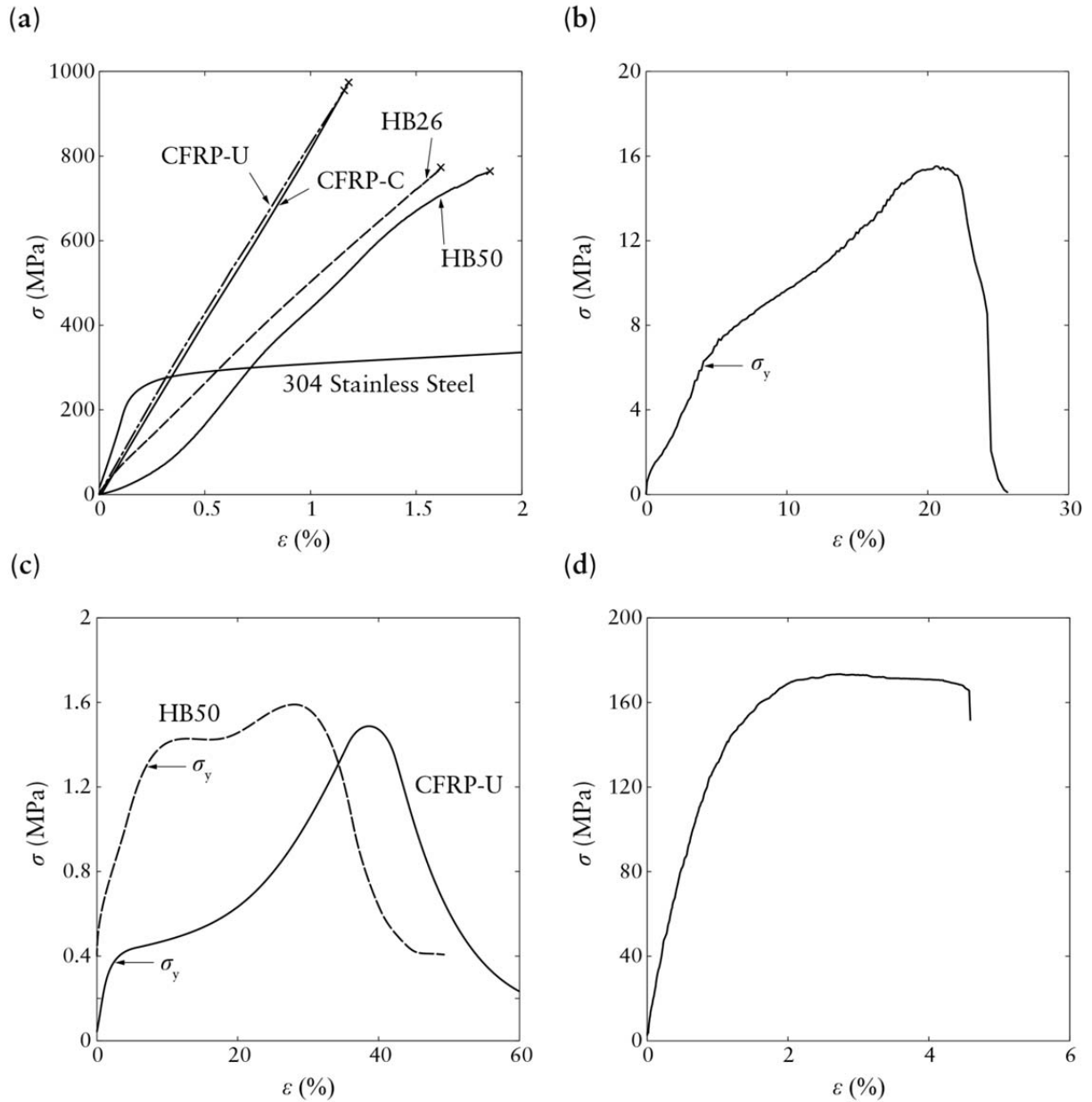


Fig. 3: The measured tensile stress versus strain responses of the (a) CFRP and UHMWPE laminates in the $0^\circ/90^\circ$ orientation as well as the 304 stainless steel. The corresponding responses in the $\pm 45^\circ$ orientation for the (b) HB26, (c) HB50 and CFRP-U and (d) CFRP-C composites. All the response are for an applied strain rate of 10^{-3} s^{-1} . The matrix yield strength is indicated on (b) to (d) by σ_y .

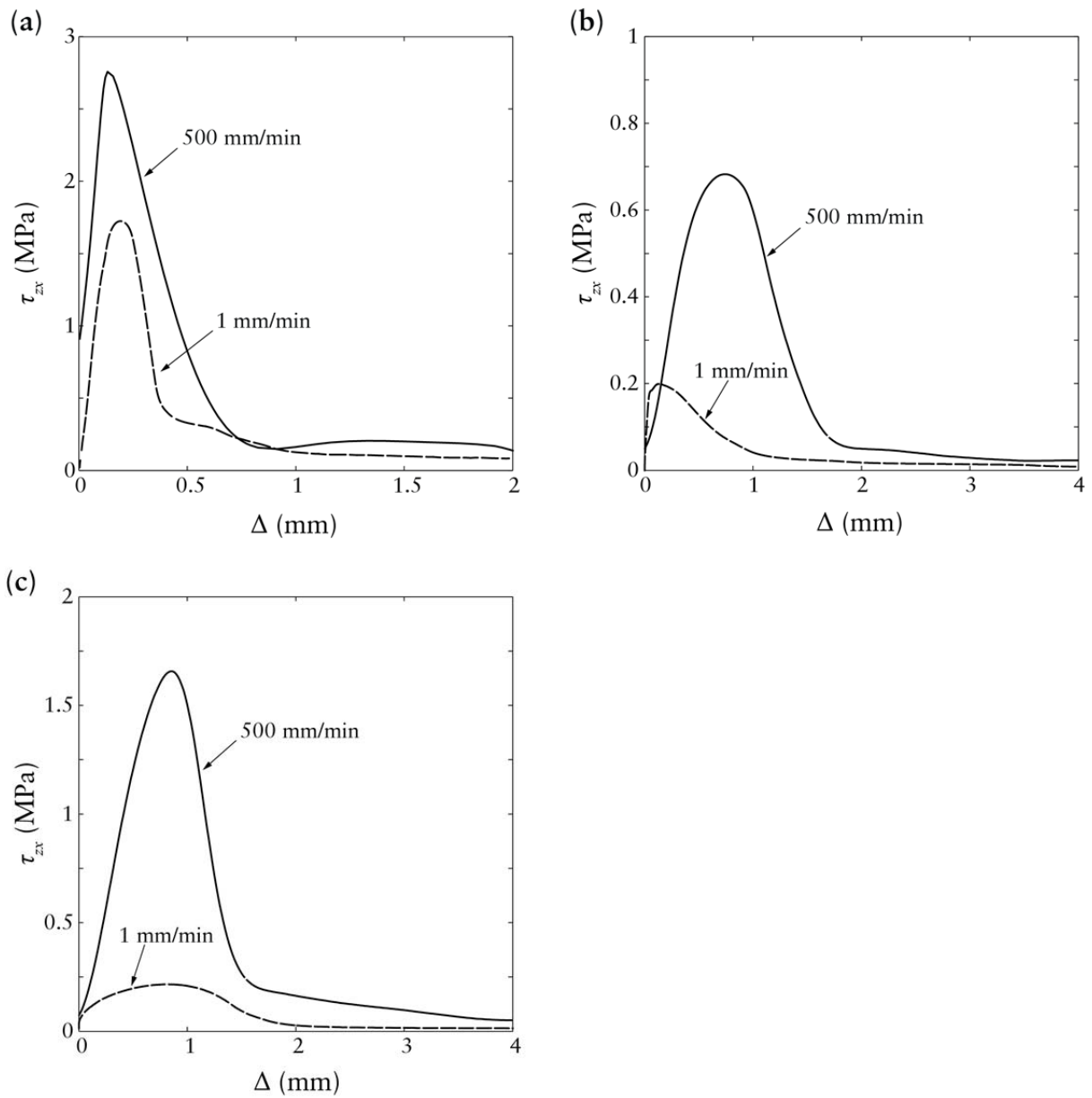


Fig. 4: The measured inter-laminar shear stress τ_{zx} versus applied shear displacement Δ responses of the (a) the HB26, (b) HB50 and (c) CFRP-U laminates at applied displacement rates of 1 mm/min and 500 mm/min. The tests were performed using the double-notch shear specimens sketched in Fig. 2b.

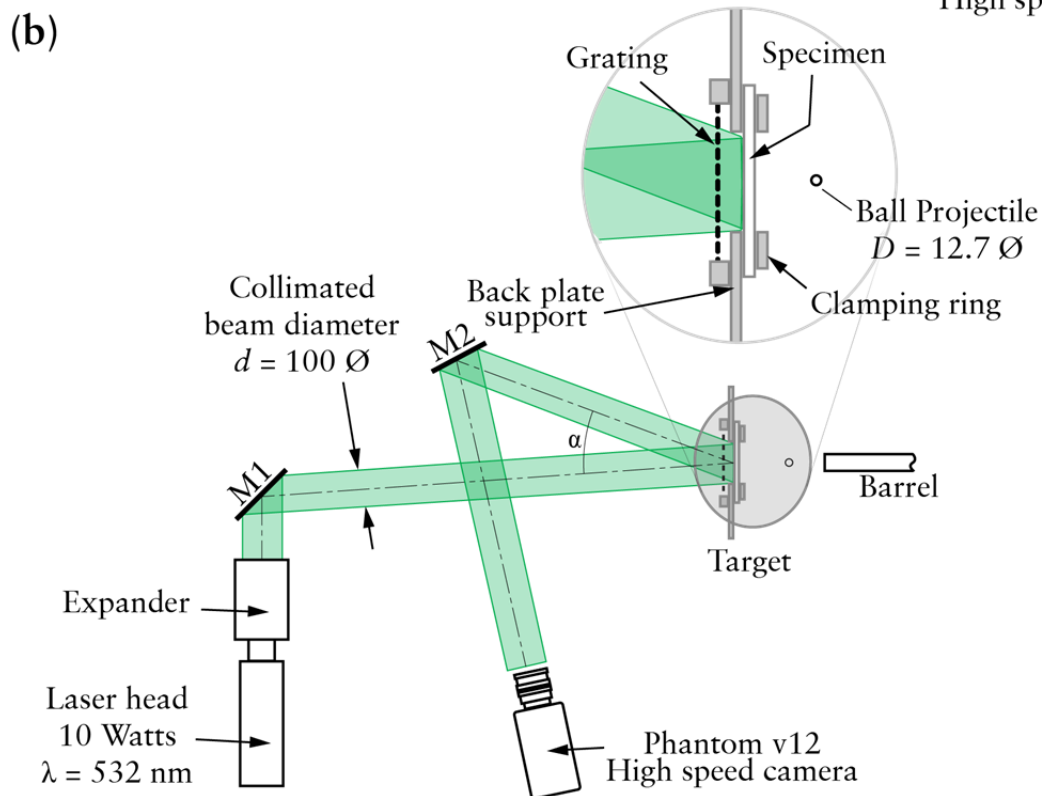
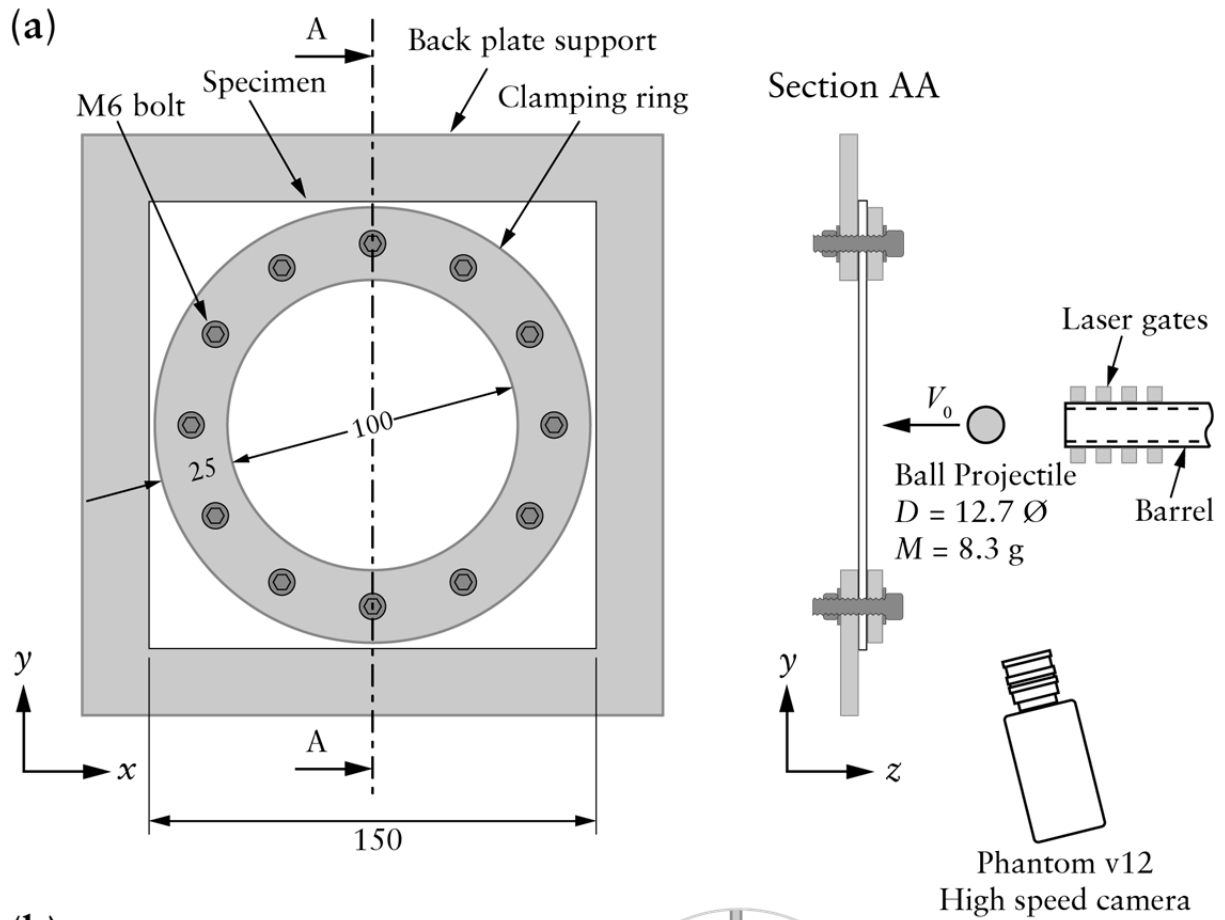


Fig. 5: (a) Plan and side view of the impact test apparatus illustrating the test set-up and the clamping arrangement. (b) Sketch showing the optical set-up used in the dynamic shadow moiré measurements. All dimensions are in mm.

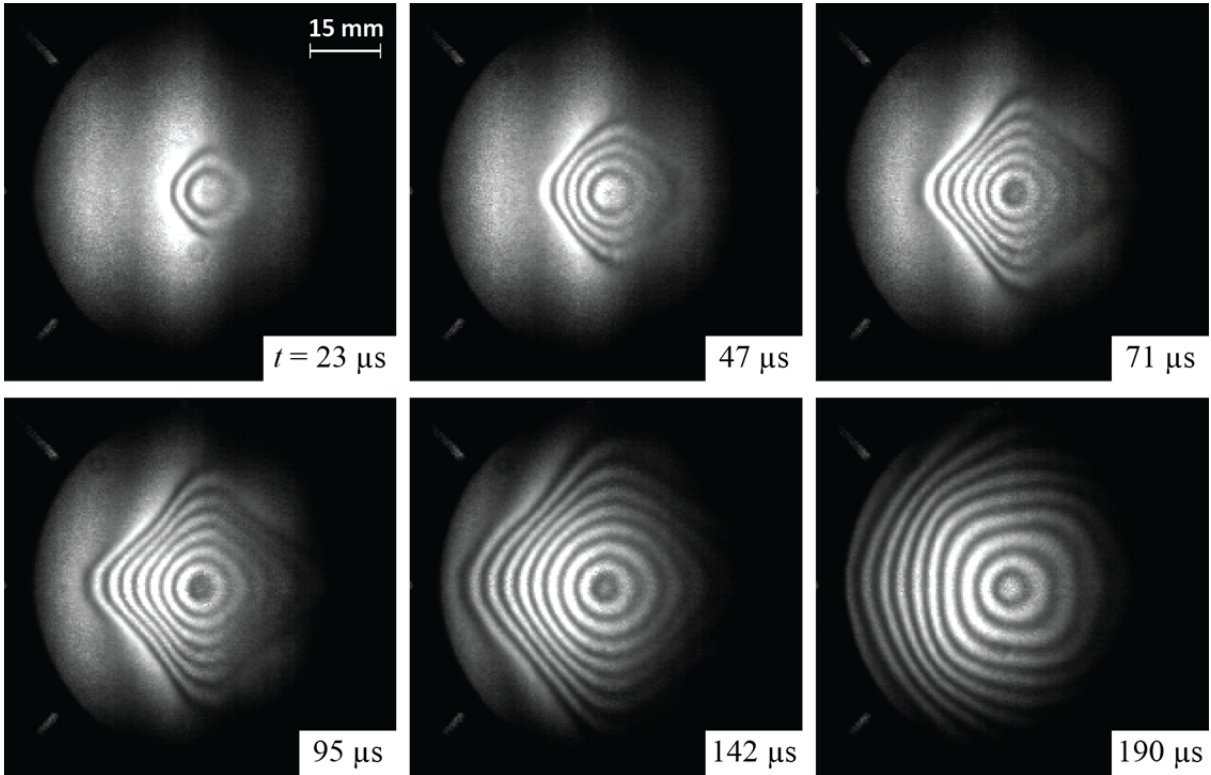


Fig. 6: Example of moiré interference fringe patterns observed during the deformation of the HB26 plate impacted at $V_0 = 250 \text{ ms}^{-1}$ by a 8.3 g steel ball. Time t as measured after the instant of impact is included on each image. Each fringe corresponds of an out-of-plane displacement of 1.58 mm. The fibres are vertically and horizontally aligned.

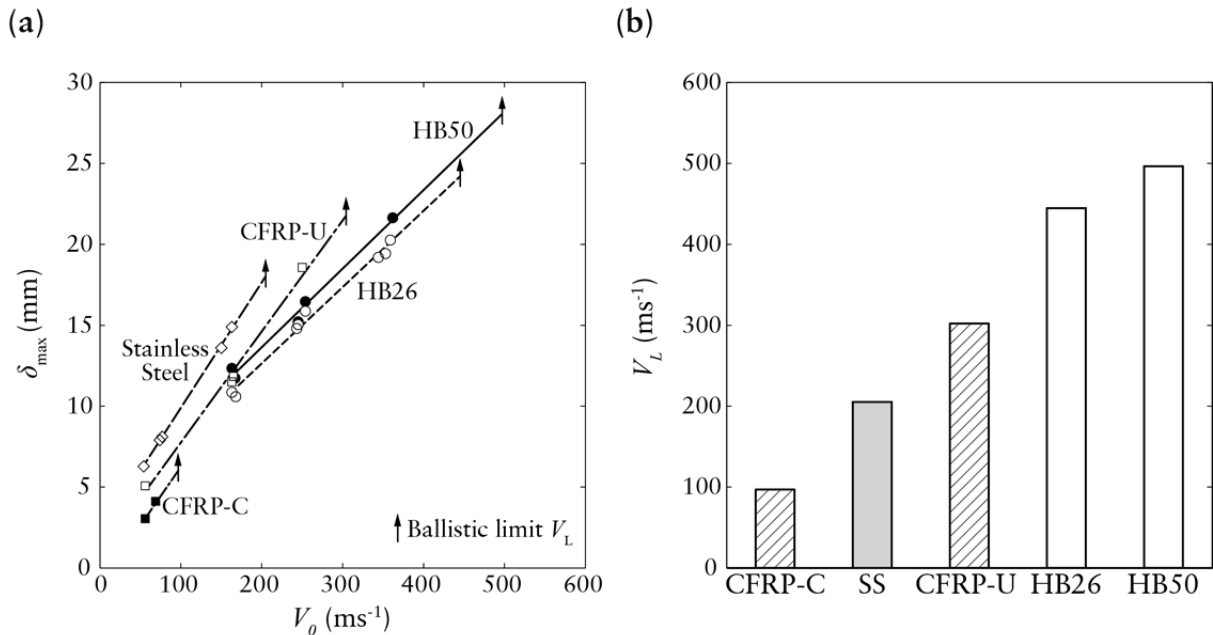


Fig. 7: The maximum mid-span deflection δ_{\max} of the plate as a function of the impact velocity V_0 of the 8.3 g steel projectile. (b) A summary of the ballistic limit V_L of the 5 plate types tested here impacted by the 8.3 g steel projectile.

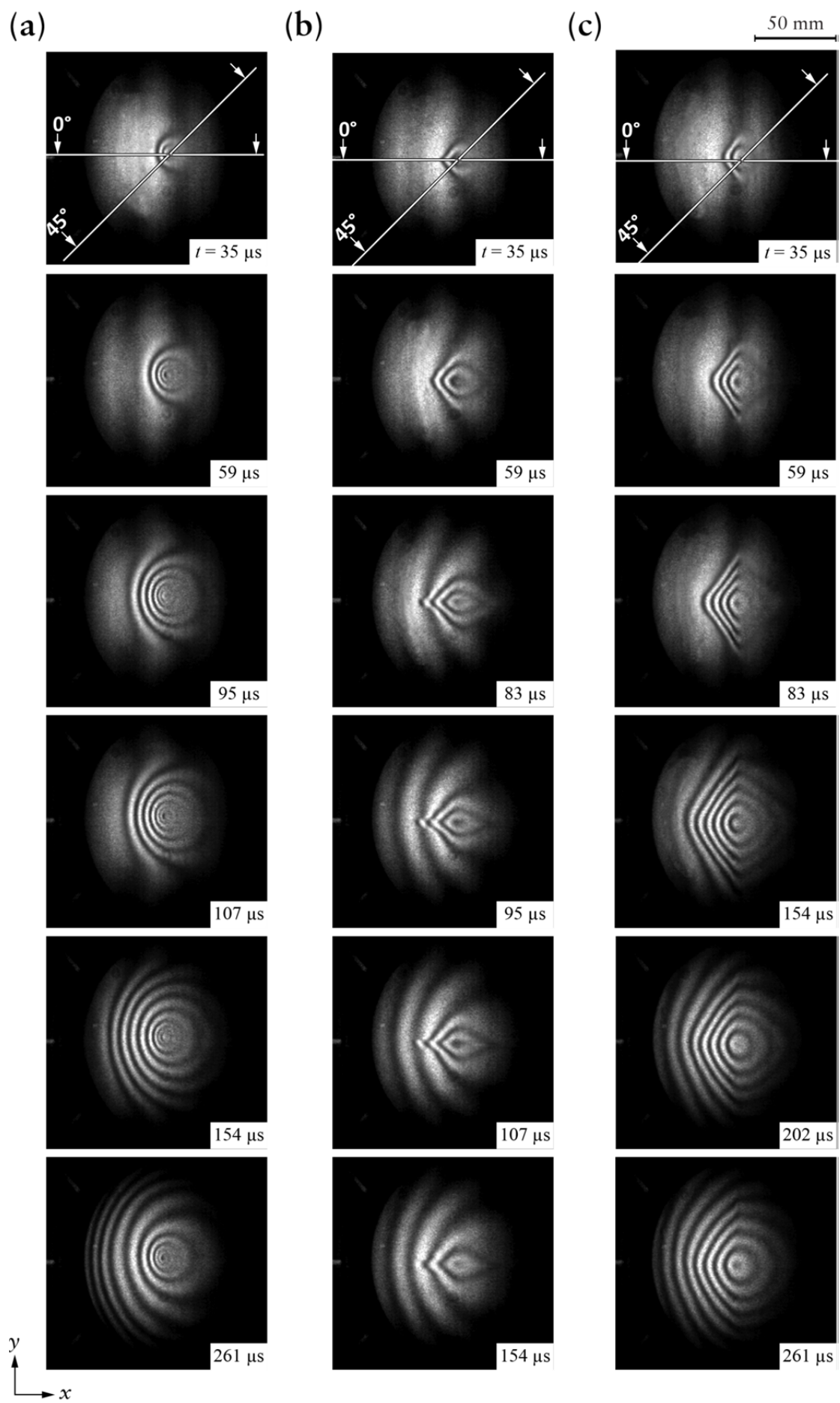


Fig. 8: Montages of moiré interference fringes during deformation of the (a) stainless steel, (b) CFRP-C and (c) CFRP-U plates at impacted $V_0 = 54 \text{ ms}^{-1}$ by the 8.3 g steel projectile. Time t as measured after the instant of impact is included on each image and the 0° and 45° sections are marked in the first image in each case. Each fringe corresponds of an out-of-plane displacement of 0.67 mm.

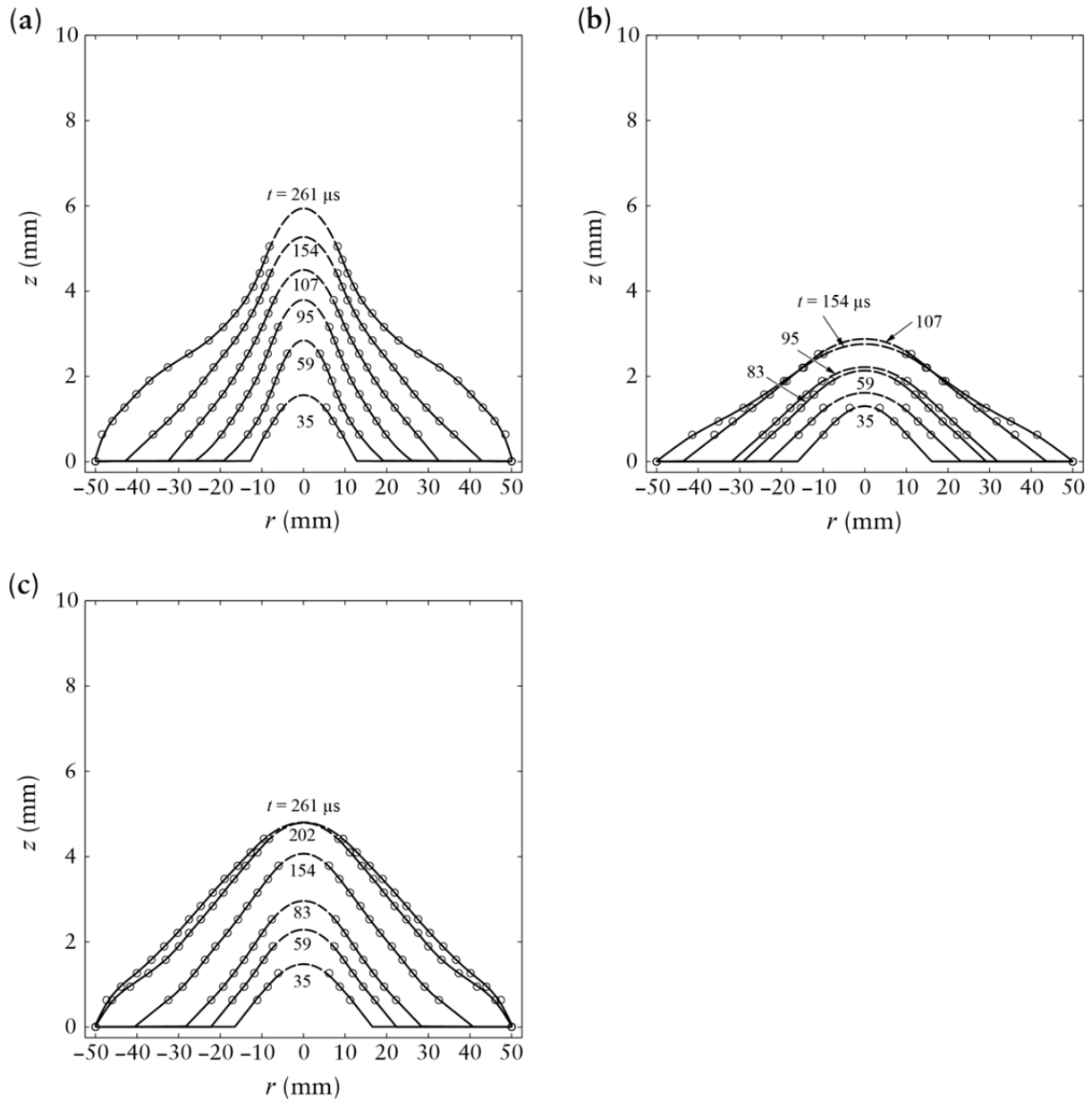


Fig. 9: The measured transient profiles for the (a) stainless steel, (b) CFRP-C and (c) CFRP-U plates along the 0° section. The profiles are extracted from the moiré fringes in Fig. 8 for the plates impacted at $V_0 = 54 \text{ ms}^{-1}$ by the 8.3 g steel ball. Time t as measured after the instant of impact is included on each figure.

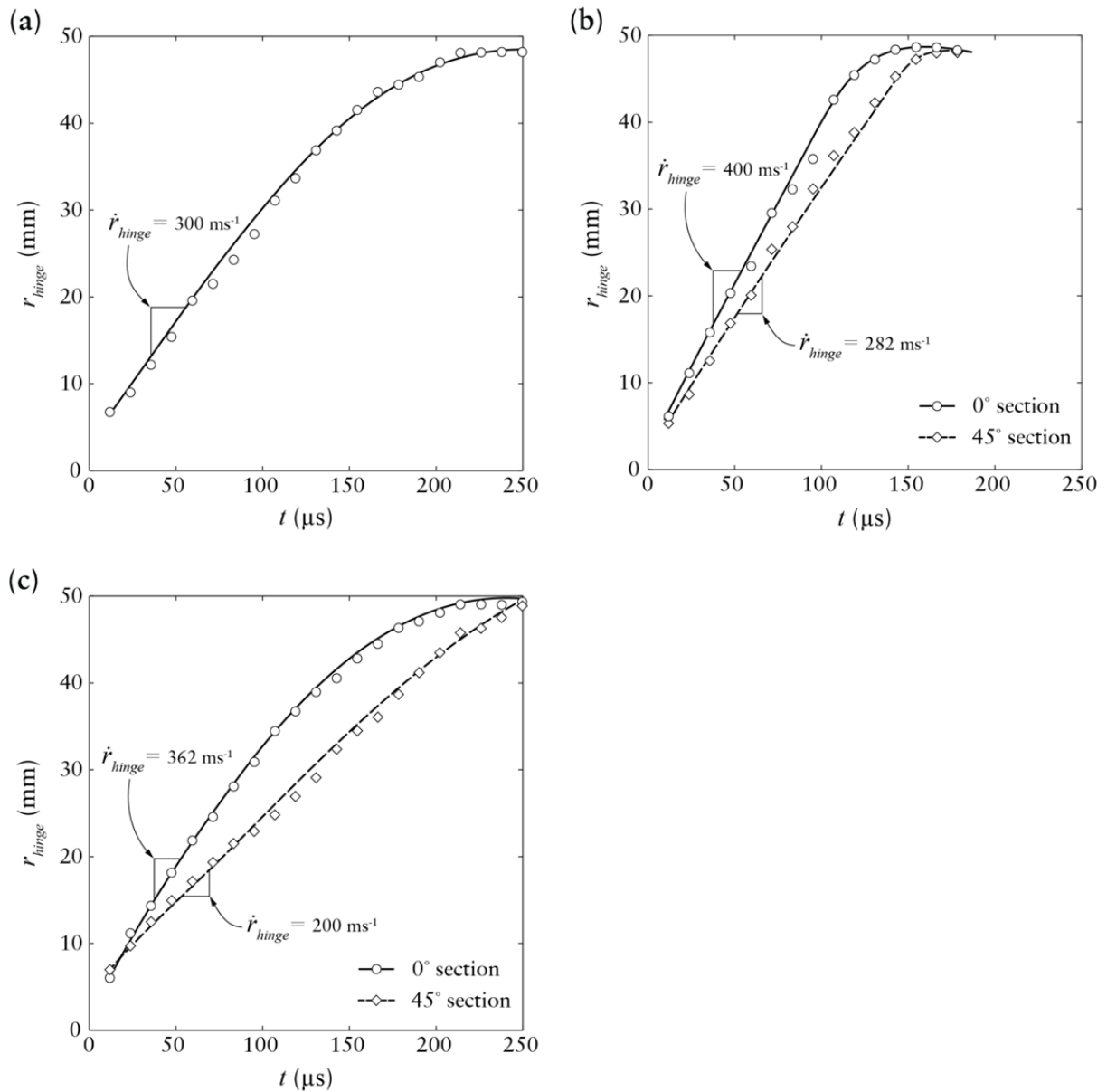


Fig. 10: The time evolution of the hinge location r_{hinge} in the (a) stainless steel, (b) CFRP-C and (c) CFRP-U plates impacted at $V_0 = 54 \text{ ms}^{-1}$ by the 8.3 g steel ball. Data is shown for the CFRP plates along both 0° and 45° sections marked in Fig. 8 with time t as measured after the instant of impact.

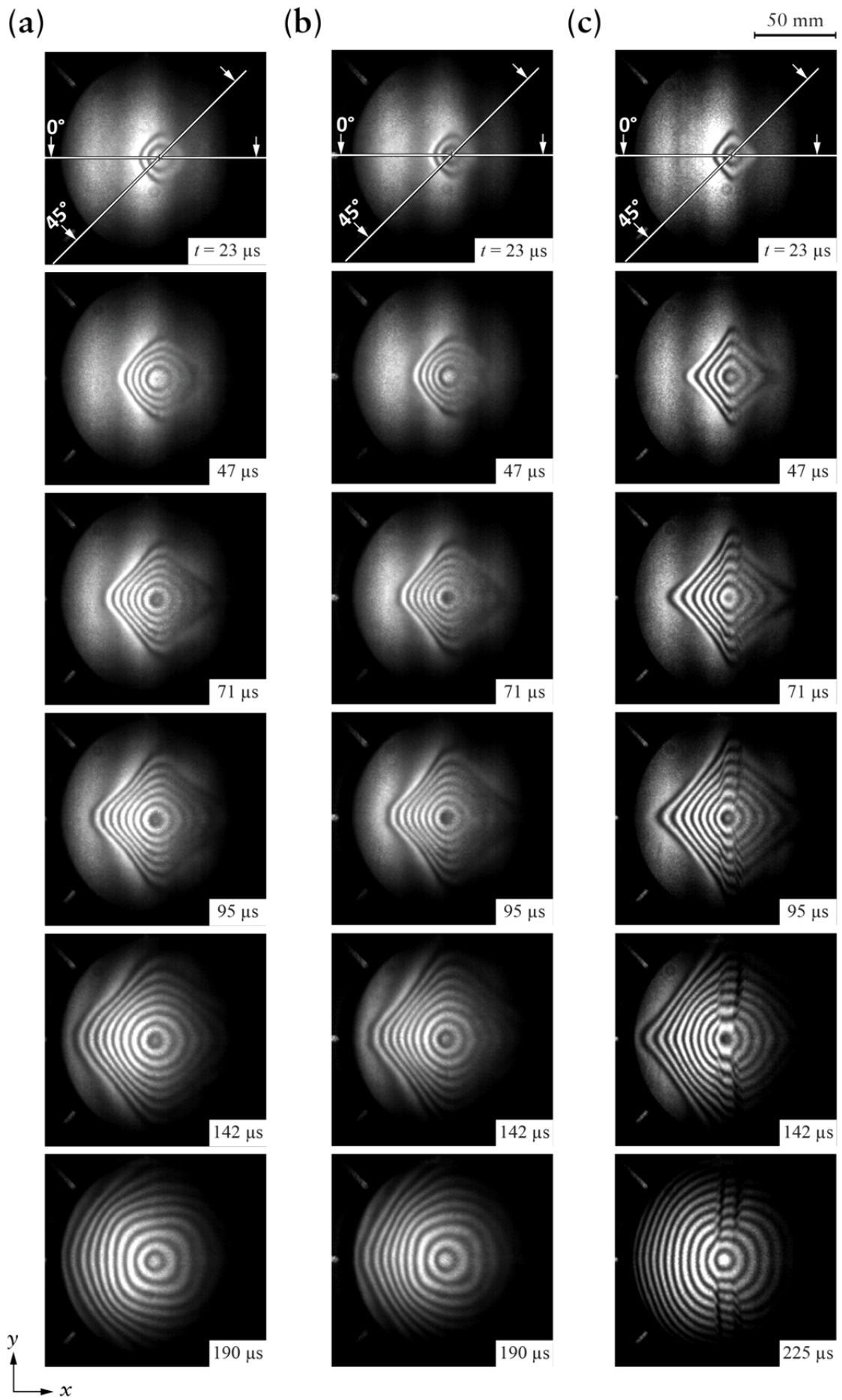


Fig. 11: Montages of moiré interference fringes during deformation of the (a) HB26 (b) HB50 and (c) CFRP-U plates at impacted $V_0 = 250 \text{ ms}^{-1}$ by the 8.3 g steel projectile. Time t as measured after the instant of impact is included on each image and the 0° and 45° sections are marked in the first image in each case. Each fringe corresponds of an out-of-plane displacement of 1.58 mm.

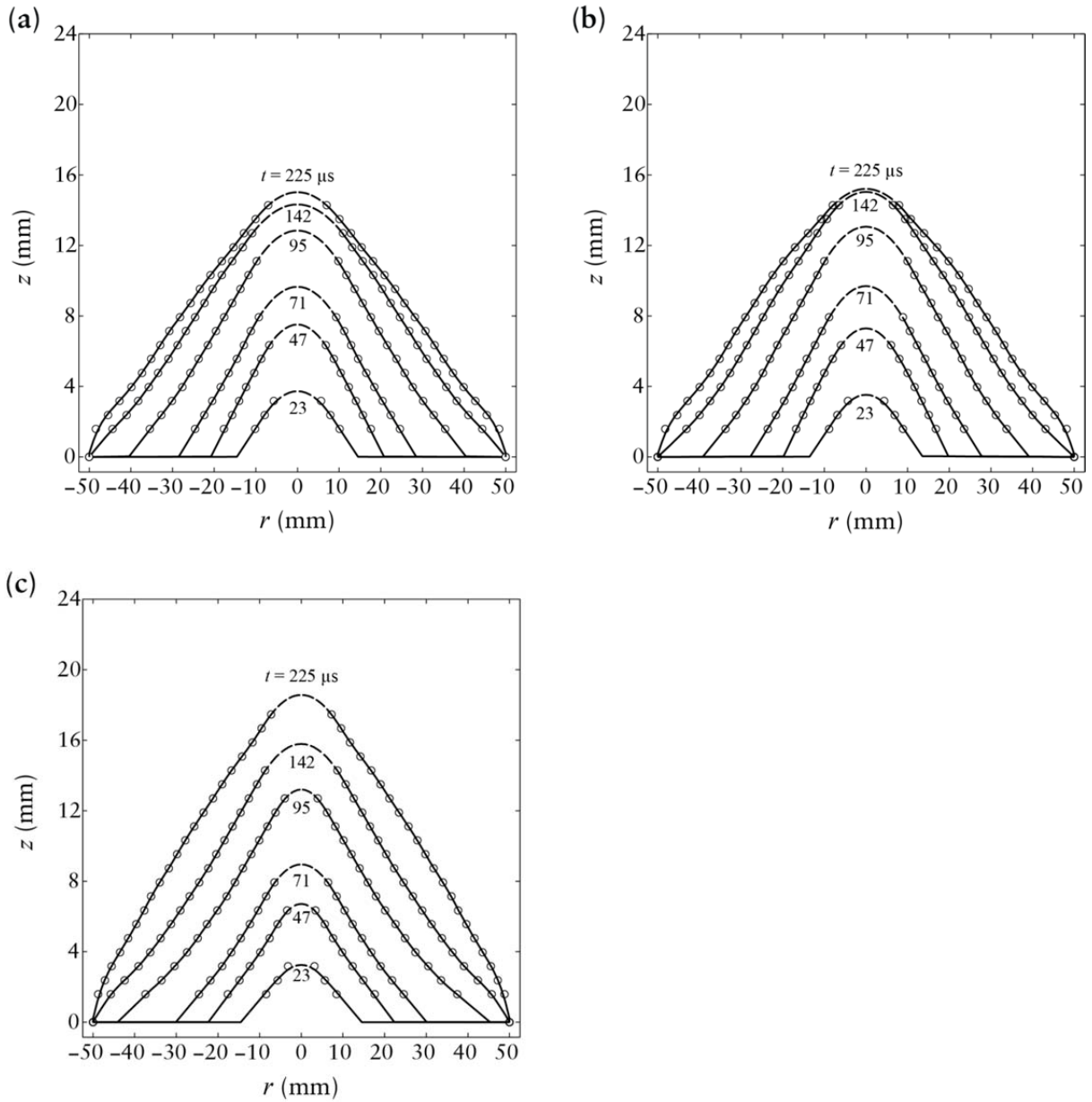


Fig. 12: The measured transient profiles for the (a) HB26, (b) HB50 and (c) CFRP-U plates along the 0° section. The profiles are extracted from the moiré fringes in Fig. 11 for the plates impacted at $V_0 = 250 \text{ ms}^{-1}$ by the 8.3 g steel ball. Time t as measured after the instant of impact is included on each figure.

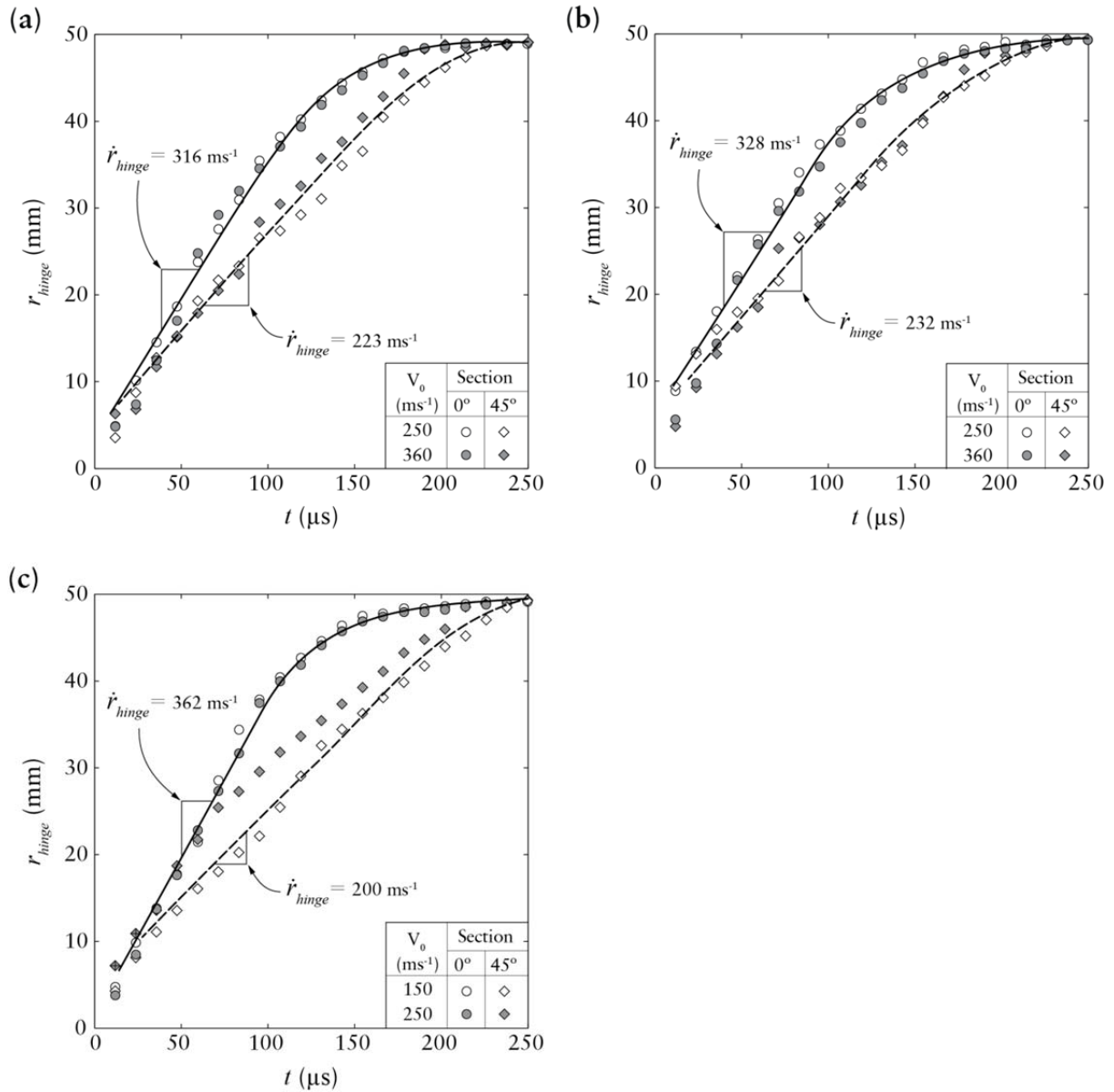
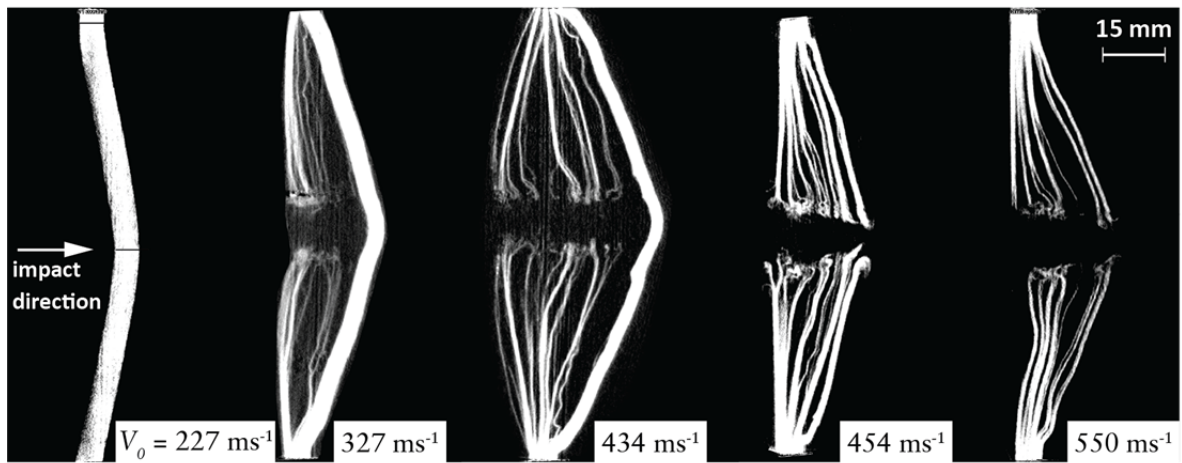
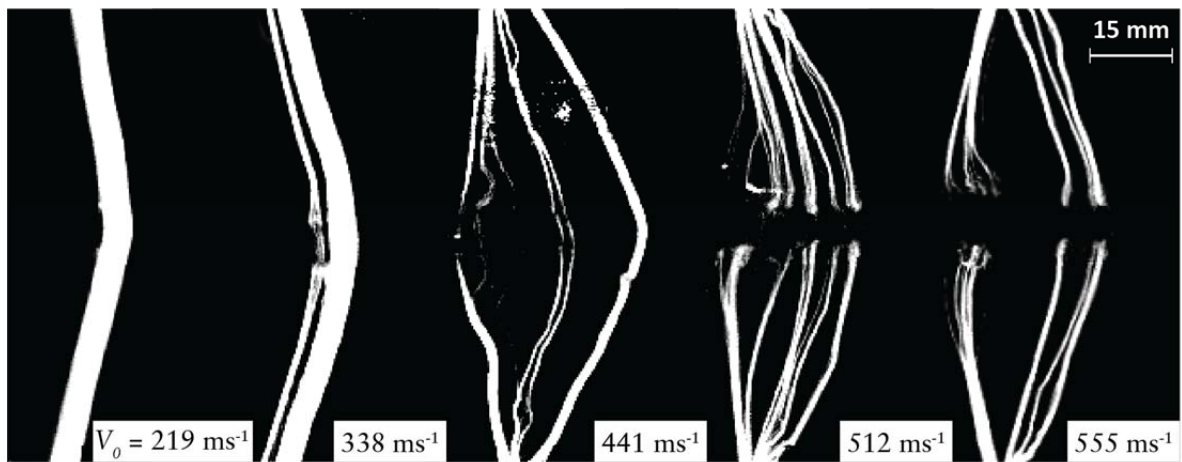


Fig. 13: The time evolution of the hinge location r_{hinge} in the (a) HB26, (b) HB50 and (c) CFRP-U plates impacted by the 8.3 g steel ball at impact velocities indicated in each figure. Data is shown along both 0° and 45° sections marked in Fig. 11 with time t as measured after the instant of impact.

(a)



(b)



(c)

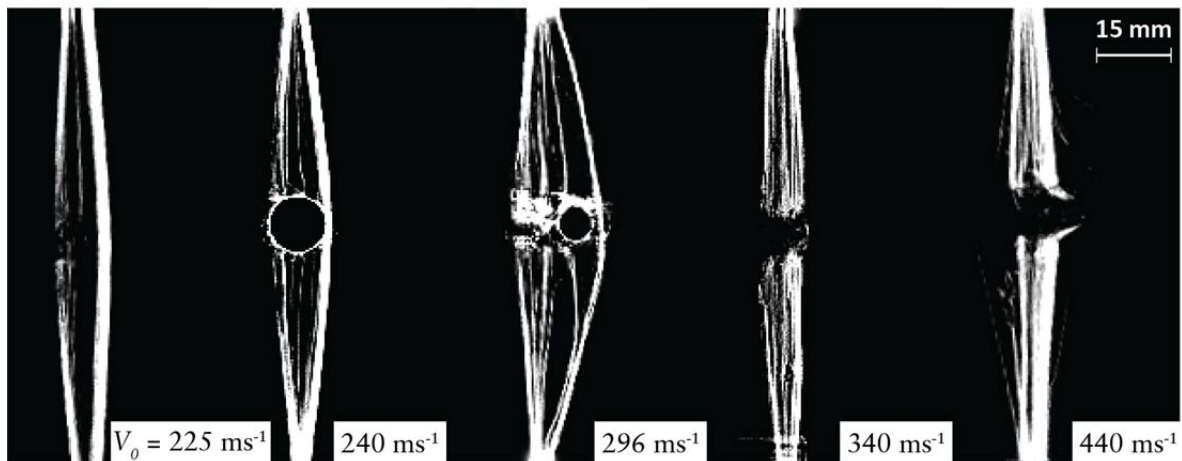


Fig. 14: X-ray images along the diametrical section of the (a) HB26, (b) HB50 and (c) CFRP-U plates impacted by the 8.3 g steel ball at selected impact velocities V_0 . Images are shown for V_0 both below and above the ballistic limit.

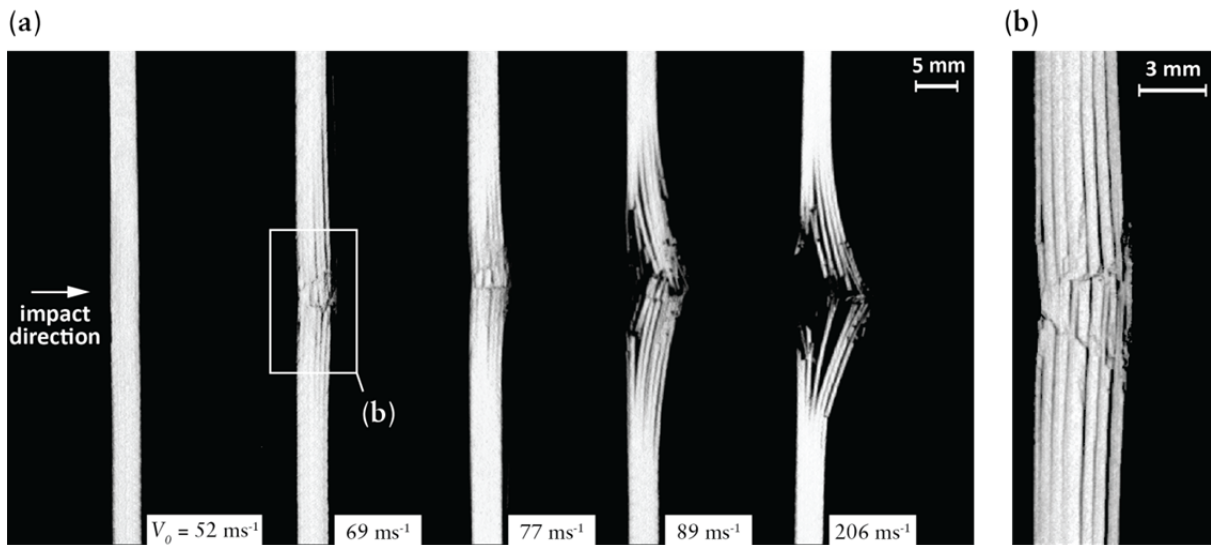


Fig. 15: (a) X-ray images along the diametrical section of CFRP-C plates impacted by the 8.3 g steel ball at selected impact velocities V_0 . Images are shown for V_0 both below and above the ballistic limit. (b) A high resolution image of the $V_0 = 69 \text{ ms}^{-1}$ CFRP-C case from (a) showing the formation of a cone crack under the projectile.

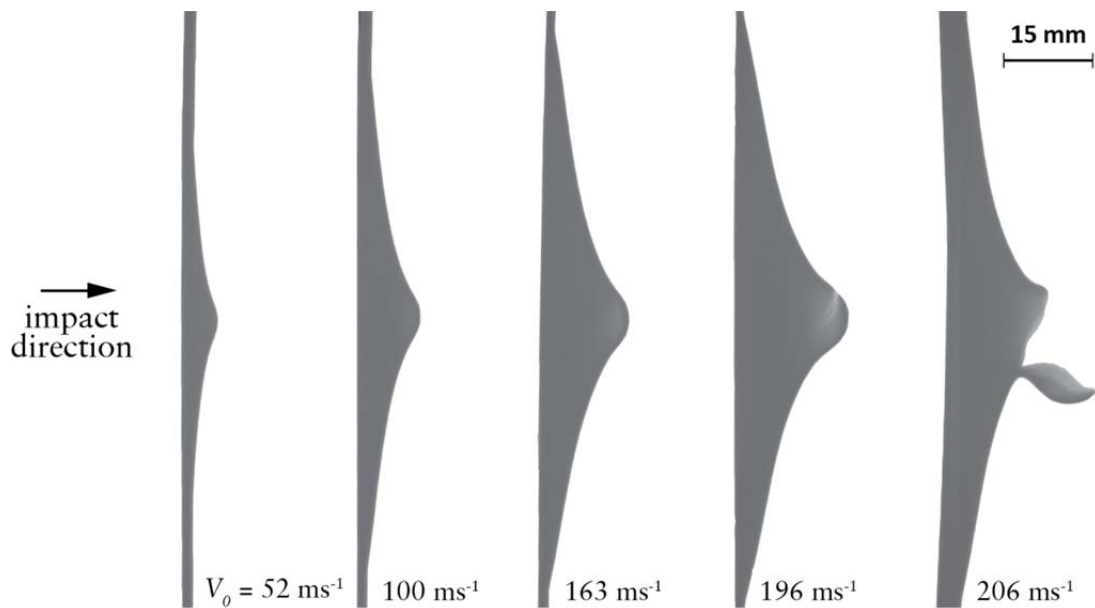


Fig. 16: X-ray images along the diametrical section of stainless steel plates impacted by the 8.3 g steel ball at selected impact velocities V_0 . Images are shown for V_0 both below and above the ballistic limit.

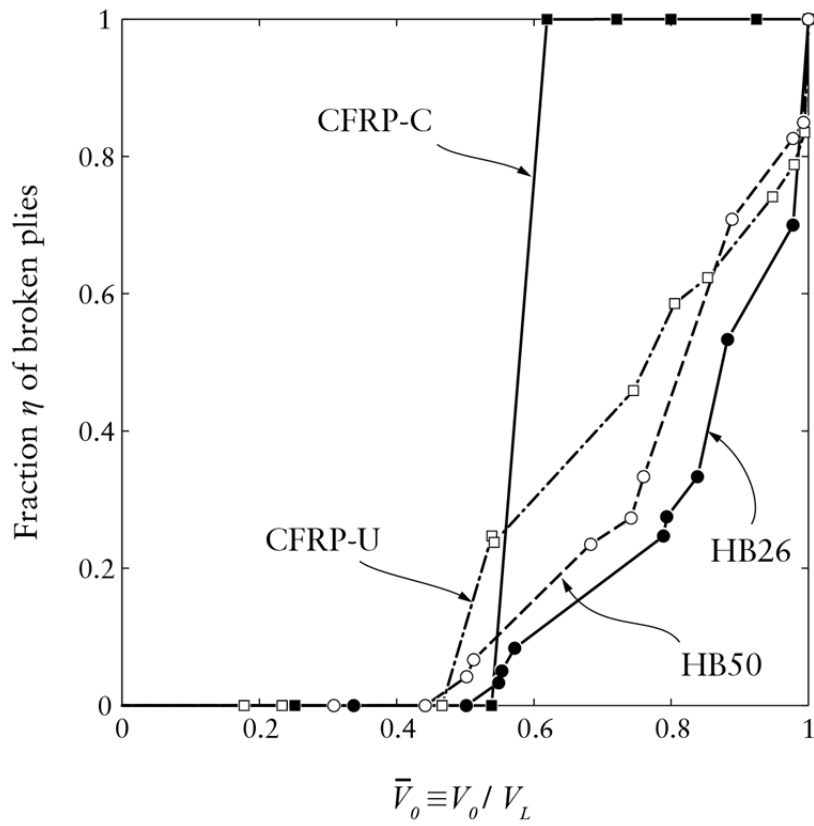


Fig. 17: The measured fraction η of broken plies as a function of normalised impact velocity $\bar{V}_0 \equiv V_0 / V_L$ for the UHMWPE and CFRP composite plates.

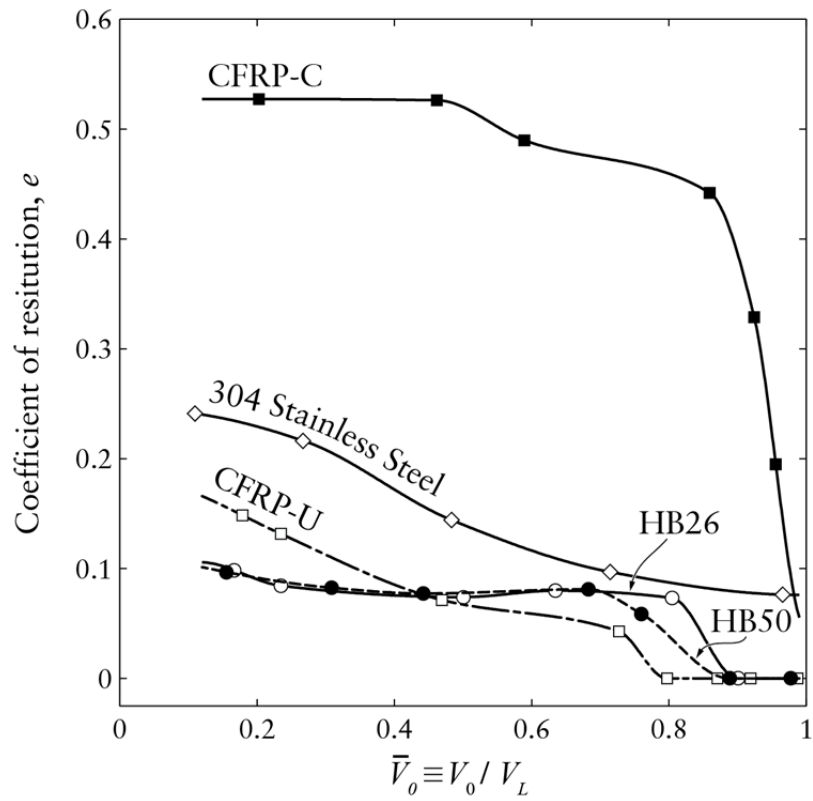


Fig. 18: The measured co-efficient of restitution e as a function of the normalised impact velocity $\bar{V}_0 \equiv V_0 / V_L$ for the UHMWPE, CFRP and stainless steel plates.

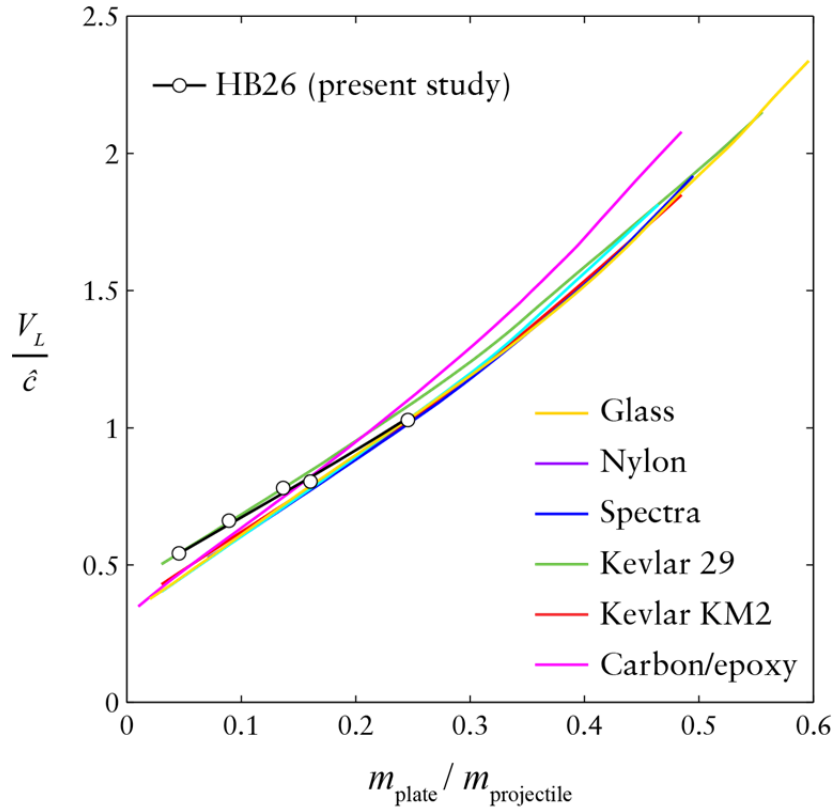


Fig. 19: The ballistic limit V_L of a range of fibre composite plates as a function of the ratio $m_{plate} / m_{projectile}$ of the areal mass of the plate and projectile. The data for V_L is taken from Cunniff [2] and normalised by \hat{c} whose values are listed in Table 2 for each of the composites. The data for HB26 measured from the current study is also included with the normalisation factor $\hat{c} = 672 \text{ ms}^{-1}$.

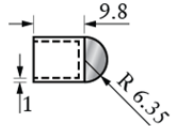
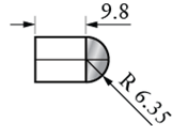
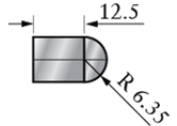
Mass M (g)	3.0	4.6	5.4	8.3	16
Geometry					
Material	Aluminum (7000 Series)	Steel front Nylon back	Steel front Nylon back	Steel	Steel

Fig. 20: Sketches of the 5 projectiles of different masses but equal projected areas used to study the ballistic Cunniff-type scaling of the HB26 composite plates.

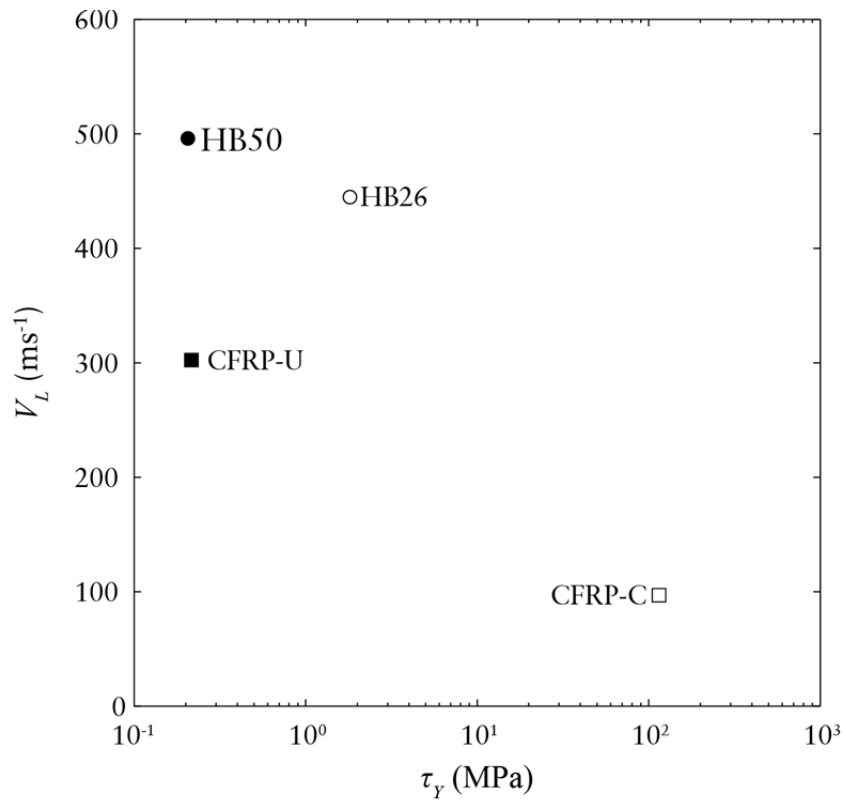


Fig. 21: The ballistic limit V_L of the UHMWPE and CFRP composite plates as a function of the shear strength τ_y . The designations of the each of the composites is indicated in the figure.